Heterogenous Si Isotopic Composition in Coastal Groundwater: Controls on Dissolved Silicon and Groundwater Discharge Along Indian Coastline

Sarath Pullyottum Kavil, Jean Riotte, Ramananda Chakrabarti, V. V. S. S. Sarma, B S K Kumar, J. Prunier, Arnaud Dapoigny, Damien Cardinal

To cite this version:

Sarath Pullyottum Kavil, Jean Riotte, Ramananda Chakrabarti, V. V. S. S. Sarma, B S K Kumar, et al.. Heterogenous Si Isotopic Composition in Coastal Groundwater: Controls on Dissolved Silicon and Groundwater Discharge Along Indian Coastline. Global Biogeochemical Cycles, 2025, 39 (8), ⟨10.1029/2025gb008706⟩. ⟨hal-05272711⟩

HAL Id: hal-05272711

https://hal.science/hal-05272711v1

Submitted on 22 Sep 2025

HAL is a multi-disciplinary open access archive for the deposit and dissemination of scientific research documents, whether they are published or not. The documents may come from teaching and research institutions in France or abroad, or from public or private research centers.

L'archive ouverte pluridisciplinaire **HAL**, est destinée au dépôt et à la diffusion de documents scientifiques de niveau recherche, publiés ou non, émanant des établissements d'enseignement et de recherche français ou étrangers, des laboratoires publics ou privés.

Distributed under a Creative Commons CC BY 4.0 - Attribution - International License

Check for updates

ADVANCING EARTH AND SPACE SCIENCES

Global Biogeochemical Cycles

RESEARCH ARTICLE
10.1029/2025GB008706

Key Points:

- The highest groundwater δ^{30}Si variability (from −1.1 to 4.5‰) observed in alluvial aquifers on the Indian coast
- No difference in δ^{30}Si between different aquifer lithologies, low rainfall regions exhibits heavier δ^{30}Si likely due to agriculture return flow
- The Si supply from fresh submarine groundwater discharge to the North Indian Ocean is <1% of riverine input, and is 0.8‰ lighter on average

Supporting Information:

Supporting Information may be found in the online version of this article.

Correspondence to:

S. Pullyottum Kavil,
sarathp39@gmail.com

Citation:

Pullyottum Kavil, S., Riotte, J., Chakrabarti, R., Sarma, V. V. S. S., Kumar, B. S. K., Prunier, J., et al. (2025). Heterogenous Si isotopic composition in coastal groundwater: Controls on dissolved silicon and groundwater discharge along Indian coastline. *Global Biogeochemical Cycles*, *39*, e2025GB008706. https://doi.org/10.1029/2025GB008706

Received 8 JUN 2025
Accepted 5 AUG 2025
Corrected 5 SEP 2025

This article was corrected on 5 SEP 2025. See the end of the full text for details.

Author Contributions:

Conceptualization: Sarath Pullyottum Kavil, Jean Riotte, Ramananda Chakrabarti, V. V. S. S. Sarma, Damien Cardinal
Data curation: Sarath Pullyottum Kavil, V. V. S. S. Sarma, J. Prunier

© 2025. The Author(s).
This is an open access article under the terms of the Creative Commons Attribution License, which permits use, distribution and reproduction in any medium, provided the original work is properly cited.

Heterogenous Si Isotopic Composition in Coastal Groundwater: Controls on Dissolved Silicon and Groundwater Discharge Along Indian Coastline

Sarath Pullyottum Kavil[1,2], Jean Riotte[3,4], Ramananda Chakrabarti[5,6], V. V. S. S. Sarma[7], B. S. K. Kumar[7], J. Prunier[3], Arnaud Dapoigny[8], and Damien Cardinal[1]

[1]LOCEAN-IPSL, Sorbonne Universite-IRD-CNRS-MNHN, Paris, France, [2]Now at: IGV, Stockholm University, Stockholm, Sweden, [3]GET-OMP, IRD, Toulouse, France, [4]Indo-French Cell for Water Sciences, ICWAR, IRD, Indian Institute of Science, Bangalore, India, [5]Centre for Earth Sciences, Indian Institute of Science, Bangalore, India, [6]Interdisciplinary Centre for Water Research, Indian Institute of Science, Bangalore, India, [7]CSIR-National Institute of Oceanography, Regional Centre, Visakhapatnam, India, [8]Laboratoire des Sciences du Climat et de l'Environnement, LSCE-IPSL, CEA-CNRS-UVSQ-Université, Gif-sur-Yvette, France

Abstract We report stable silicon isotope ratio (δ^{30}Si) of over 80 groundwater samples collected along the Indian coast, spanning a wide range of aquifer lithologies (alluvial, basalt, metamorphic, laterite and limestone), climate (semi-arid to tropical wet) and land use settings. Indian coastal groundwater exhibits large spatial variability in dissolved silicon (DSi) (80–1350 μM) and δ^{30}Si values (−1.1‰ to 4.5‰). On average, the δ^{30}Si value of the Indian coastal groundwater (0.8 ± 1.1‰, 1SD, $n = 85$) is comparable to published groundwater globally (0.8 ± 0.8‰, $n = 117$), and significantly lower than Indian riverine δ^{30}Si composition. The coastal groundwater δ^{30}Si values do not show any dependence on regional aquifer lithology. However, the permeable coastal alluvial groundwaters exhibit the highest variability in DSi and δ^{30}Si, likely acquiring signatures of shallow surface/subsurface processes through mixing. A broad negative correlation between δ^{30}Si values and the Ge/Si ratio is best explained by the partitioning of Si into secondary minerals phases within the weathering zone. The majority of coastal groundwater follows a steady-state model evolution, indicating a dynamic equilibrium between Si supply and the formation of secondary phases. In regions of low annual rainfall, groundwater irrigation can lead to infiltration of return flow water to aquifer systems, leading to their heavy δ^{30}Si values. The fresh submarine groundwater discharge along the Indian coast is estimated to be 2.1 GmolSi yr^{-1}, which is less than 1% of the riverine Si flux to the North Indian Ocean and 0.3% of the global fresh groundwater Si flux.

1. Introduction

Continental silicate weathering regulates the atmospheric CO_2 consumption over geological time scales and releases dissolved silicon (DSi) in rivers, and subsequently to oceans, where it is incorporated in marine silicifiers, dominated by diatoms in the present day (Berner et al., 1983; Maldonado et al., 2019). Marine diatoms are responsible for almost 40% of marine primary productivity, driving the deep-sea export of organic carbon through biological carbon pumps (Field et al., 1998; Tréguer et al., 2018). Submarine groundwater discharge (SGD) is considered to be the second largest source of DSi to the ocean, contributing up to 25% of the total silicon flux (Rahman et al., 2019; Tréguer et al., 2021). SGD is ubiquitous in most shorelines and consists of fresh terrestrial groundwater (fresh SGD) and recycled saline groundwater (saline SGD) (Burnett et al., 2006; Chakrabarti et al., 2018; Moore et al., 2010). The fresh SGD originates from shallow and/or deep coastal aquifers, inheriting signatures of terrestrial weathering and anthropogenic inputs. The fresh SGD is primarily driven by a positive hydraulic gradient from the continent (Taniguchi et al., 2002). The saline SGD results from the recirculation of seawater into coastal sediments and aquifers, which can incorporate signatures of water-rock interactions in subsurface regions (Moore et al., 2010). Globally, the SGD DSi flux to the ocean is estimated to be 3.8 Tmol/yr, out of which almost 80% occurs as saline SGD (Cho et al., 2018; Rahman et al., 2019). However, groundwater discharge is often patchy and diffuses spatially, and the discharge timescales vary from hours to millennia (Bratton, 2010; Moore et al., 2010). Thus, the measurement of magnitude and associated chemical fluxes of SGD is a challenging problem and requires extensive sampling of coastal and offshore groundwater reserves. In addition to DSi, SGD is now known to be a significant source of nutrients such as nitrate and phosphorus, impacting coastal biogeochemistry (Santos et al., 2021).

Formal analysis: Sarath Pullyottum Kavil, Jean Riotte, J. Prunier, Arnaud Dapoigny, Damien Cardinal
Funding acquisition: Ramananda Chakrabarti, V. V. S. S. Sarma
Investigation: Sarath Pullyottum Kavil, Jean Riotte, Ramananda Chakrabarti, B. S. K. Kumar, J. Prunier, Damien Cardinal
Methodology: Sarath Pullyottum Kavil, Jean Riotte, Ramananda Chakrabarti, V. V. S. S. Sarma, B. S. K. Kumar, J. Prunier, Arnaud Dapoigny, Damien Cardinal
Project administration: Jean Riotte, Ramananda Chakrabarti, V. V. S. S. Sarma, Damien Cardinal
Resources: Ramananda Chakrabarti, V. V. S. S. Sarma, B. S. K. Kumar, J. Prunier
Supervision: Ramananda Chakrabarti, V. V. S. S. Sarma
Validation: Sarath Pullyottum Kavil, Jean Riotte, Arnaud Dapoigny, Damien Cardinal
Visualization: Sarath Pullyottum Kavil
Writing – original draft: Sarath Pullyottum Kavil
Writing – review & editing: Sarath Pullyottum Kavil, Jean Riotte, Ramananda Chakrabarti, V. V. S. S. Sarma, B. S. K. Kumar, Damien Cardinal

In terrestrial environments, groundwater forms an intermediate between soil and river water, dwarfing all other hydrological systems in terms of the total volume of freshwater storage (Gleeson et al., 2015). The DSi in groundwater inherits its signature from surface and subsurface water-soil-plant interactions and can further undergo weathering reactions in the aquifers before discharging into rivers and oceans (Worthington et al., 2016). During weathering of primary silicate minerals, the silicon is partitioned between secondary phases and porewater solution as dissolved silicon. The solubilized silicon can further undergo biotic uptake by plants and siliceous organisms and adsorption onto Fe oxy-hydroxide phases (Opfergelt & Delmelle, 2012). Both the abiotic and biotic processes of Si uptake are associated with significant isotopic fractionations, favoring the preferential incorporation of the lighter ^{28}Si into the solid phase, making the residual solution heavier in silicon isotopic composition (Frings et al., 2016; Opfergelt & Delmelle, 2012). The Ge/Si ratio is routinely coupled with δ^{30}Si measurements to distinguish between secondary clay formation and plant uptake, where Ge is known to be preferentially incorporated and/or adsorbed into secondary minerals (high Ge/Si), while plant phytoliths exhibit low Ge/Si (Delvigne et al., 2009; Derry et al., 2005; Kurtz et al., 2002; Mortlock & Frohlich, 1987). Thus, combining the Ge/Si ratio with δ^{30}Si values can be beneficial to understanding the extent of biogenic versus weathering control on Si cycling on Earth's surface (Frings, Schubring, et al., 2021). The groundwater δ^{30}Si values for globally distributed samples measured so far spans from −1.5 to +2.6‰; high δ^{30}Si values are generally attributed to incongruent silicate weathering (upper continental crust, UCC, δ^{30}Si of −0.25 ± 0.16‰, Savage et al., 2013), while lighter isotopic composition is attributed to the dissolution of secondary phases, such as clays and silcretes (e.g., Georg, West, et al., 2009, Georg, Zhu, et al., 2009; Pogge von Strandmann et al., 2014). The average δ^{30}Si value of global groundwater (0.8 ± 0.8‰, $n = 117$) is lower than that of reported average of global river water (1.25 ± 0.7‰, $n = 557$, Ehlert, Reckhardt, et al., 2016; Ehlert, Doering, et al., 2016; Frings et al., 2016, Martin et al., 2021, Kavil et al., 2024). The distinct isotopic composition and large Si fluxes as SGD make groundwater an important reservoir of Si, which can potentially alter the magnitude and composition of Si fluxes to the ocean in glacial-interglacial timescales (Tréguer et al., 2021). Despite large heterogeneity in isotopic composition, complexity in controlling processes and direct impact on riverine and oceanic elemental budget, groundwater Si cycling largely remains overlooked.

The Indian coastline stretches for almost 7,500 km, hosting diverse aquifer systems, including gneisses, basalts, limestones and recent alluvium, with precipitation levels ranging from <500 mm/yr to >2,500 mm/yr (CGWB, 2012). Previous works have reported evidence of total SGD in both the East and West coasts of India using various elemental and isotopic tracers, with estimated flux up to 150×10^9 m^3/yr, almost 30% of annual discharge of Indian monsoonal rivers (Chakrabarti et al., 2018; Das et al., 2025; Krishna et al., 2016; Rahaman & Singh, 2012; Rengarajan & Sarma, 2015). Almost 57% of the Indian coastal area has groundwater table depth between 0 and 10 m above sea level, exhibiting a high terrestrial hydraulic gradient conducive to fresh SGD (Luijendijk et al., 2020; Manivannan & Elango, 2019). Groundwater in extrusive igneous and granitic lithologies can acquire high DSi through silicate weathering, increasing the net SGD DSi delivery to the coast (Rahman et al., 2019). The SGD Si flux estimated on the East coast of India accounts for almost 17% and 40% of Si delivered through the Godavari and Ganges-Brahmaputra rivers, respectively (Georg, Zhu, et al., 2009; Rengarajan & Sarma, 2015). Despite increasing evidence of substantial SGD water fluxes through Indian coasts, we lack an understanding of the variability and drivers of groundwater DSi composition. The present work aims to expand the global groundwater δ^{30}Si data set by analyzing more than 80 coastal groundwater spread along the Indian subcontinent, encompassing a wide range of aquifer lithologies and precipitation zones. We investigated (a) the variability in DSi and δ^{30}Si signatures of peninsular Indian coastal groundwater, (b) the potential sources and/or processes driving Si cycling in groundwater, and (c) the impact of SGD Si fluxes on the North Indian Ocean.

2. Materials and Methods

2.1. Study Site Description

Indian coastline covers almost 7,500 km, bounded by the Arabian Sea in the West, the Bay of Bengal in the East and the Indian Ocean in the South (Dimri et al., 2023; Manivannan & Elango, 2019). The aquifer systems in Indian coast is dominated by alluvium in the East, Cretaceous Deccan basalts and banded gneiss complex in the West (CGWB, 2012). Alluvium aquifers form the dominant aquifer type in India (29.8%), primarily consists of quartz, plagioclase feldspars and clays (CGWB, 2012; Shamsudduha et al., 2008). Deccan tholeiite basalts form low permeability hard rock aquifers (16.2%), and their major mineral phases include olivine, plagioclase,

19449224, 2025, 8, Downloaded from https://agupubs.onlinelibrary.wiley.com/doi/10.1029/2025GB008706 by Cochrane France, Wiley Online Library on [22/09/2025]. See the Terms and Conditions (https://onlinelibrary.wiley.com/terms-and-conditions) on Wiley Online Library for rules of use; OA articles are governed by the applicable Creative Commons License

clinopyroxenes and orthopyroxenes (Beane et al., 1986). The gneiss complex lithology (15.1%) primarily consists of quartz, biotite-chlorite and plagioclase, with the minor occurrence of amphiboles and pyroxenes (Braun et al., 2009). Most regions with Precambrian crystalline basement rocks are overlain by Tertiary sediments, laterite, and alluvium (Laluraj et al., 2007). Along the Indian coast, 57% of groundwater levels are between 0 and 10 m above the sea level and 7% of the coastal aquifers are affected by seawater intrusion (Manivannan & Elango, 2019). Major rivers discharging to the Indian coast (including Ganges, Brahmaputra, and Godavari) form extensive alluvium deposits near the coast. The Bay of Bengal receives almost 1,600 km^3 of fresh river water influx annually, while the Arabian Sea only receives 300 km^3 (Krishna et al., 2016). The rainfall in the Indian subcontinent is dominated by the summer monsoon (75%–80% of total rainfall), occurring during June to September. It is followed by North East monsoon (11% of total rainfall) from October to December (Lakshmi et al., 2019). The West coast of India constitutes the windward side of the Western Ghats mountains and receives maximal precipitation during the summer monsoon, while the northeast monsoon dominates on the East coast (Kumar et al., 1992; Rajeevan et al., 2012). Annual average rainfall on the East coast ranges from 300 to 2,500 mm, and on the West coast from 1,000 to 3,500 mm (CGWB, 2012). More than 50% of the land area in India is under cultivation, primarily composed of rice, wheat, sorghum, maize, sugarcane and barley (FAO, 2022; Gopalakrishnan & Kulkarni, 2007). Coastal states are known to be major producers of rice and sugarcane, with 40%–80% of the agricultural land cultivated using groundwater irrigation (Kumar et al., 2021). The coastal groundwaters are significantly impacted by fertilizer use in India. High concentrations of nitrate, for instance, were reported in Odisha, Andra Pradesh, Tamil Nadu, Karnataka, Goa and Gujarat (Kumar et al., 2021).

2.2. Sampling and Field Measurements

Groundwater samples were collected along the Indian coastline during the dry season in April 2017 (pre-monsoon). We sampled 86 groundwater from handpumps, open borewells and pumped borewells, mostly within a few kms from the coast. Details of the sampling locations and type of groundwater are described in Table 1. Groundwater table depths were not available as a large part of the samples consist of pumps and borewells, which are isolated from the surface. Modern borewells are reinforced using PVC as well as the casing pipes and the tubing and thus it is unlikely to be source of any Si isotope fractionation. Groundwater samples from open wells were collected using 5L Niskin bottles, and groundwater pumps were purged thoroughly before sampling to prevent sampling bias and isotopic fractionation from Si adsorption on the metal tubing. The groundwater was immediately filtered using 0.22 μm cellulose acetate filters and stored in pre-acid cleaned containers. The conductivity was measured using a conductivity meter (HI2003, accuracy ± 1%) and pH using a glass electrode (WTW, MultiLine P4). The groundwater samples are classified into different aquifer lithology based on the published aquifer system map from online Water Resources Information System (WRIS, https://indiawris.gov.in/wris) and the regional annual average precipitation data was aquired from AQUASTAT (FAO, 2022).

2.3. Elemental Concentration

Major cation concentrations (Na^+, K^+, Ca^{2+}, Mg^{2+}) were measured using ICP-OES iCap (Thermo Fischer Scientific) at GESE (Génie Environnemental Sols et Eaux, Sorbonne Université, Ivry Paris). Major anion concentrations were measured with an Ion Chromatograph (Metrohm COMPACT 861) at the Indo-French Cell for Water Sciences (IFCWS, Indian Institute of Science, Bengaluru, India). The accuracy of measurements was monitored using multiple certified reference materials (AnionWS, ION-96.4, ION 915, SUPER-05 and BIG MOOSE 02). The average precision was monitored using standard references and was better than 10%.

2.4. Dissolved Silicon and Si Isotope Analysis

Silicon concentration (DSi) was measured by spectrophotometer following the Grasshoff et al. (1999) protocol. The accuracy of measurements was assessed using the certified reference material PERADE 09 (NRC-Canada#0314). The mean value obtained from the repeated measurements of this standard ($n = 25$) was 110 ± 3 μM, that is, identical to the certified value of DSi = 110 ± 7 μM (NRC-Canada#0314). For the separation of silicon for isotopic analysis, we followed a slightly modified two-step pre-concentration method adapted from MAGIC (MAGnesium Co-precipitation technique, Hughes et al., 2011; Karl & Tien, 1992; Reynolds, 2006). To an initial volume of 10 ml of groundwater and surface water samples, we added 0.5 ml of 0.1 M $MgCl_2$ solution to match the seawater Mg concentration, following which 2% (v/v) of 1 M NaOH was added, mixed well and kept undisturbed overnight. The brucite ($Mg(OH)_2$) formed at high pH scavenges Si, which gets adsorbed onto

19449224, 2025, 8, Downloaded from https://agupubs.onlinelibrary.wiley.com/doi/10.1029/2025GB008706 by Cochrane France, Wiley Online Library on [22/09/2025]. See the Terms and Conditions (https://onlinelibrary.wiley.com/terms-and-conditions) on Wiley Online Library for rules of use; OA articles are governed by the applicable Creative Commons License

Table 1

The Sampling Details, Geochemical and Si Isotopic Composition of the Coastal Groundwater Samples

	Latitude	Longitude	Aquifer lithology	Type	pH	Conductivity µS/cm	DSi µM	δ^{30}Si ‰	1SD	Ge/Si µmol/mol	Na µM	K µM	Mg µM	Cl µM	NO3 µM	SO4 µM
GJ1	20.5981	72.9424	Basalt	Hand pump	7.12	1,120	509	4.08	0.17	0.36	5,661	32	2,070	5,527	91	596
GJ2	21.1242	72.7861	Alluvium	Pump	7.49	1,360	675	1.09	0.13	0.21	11,820	40	313	1,722	364	461
GJ3	22.2507	73.1852	Alluvium	Pump	7.13	2,110	409	3.99	0.02		5,893	50	6,205	11,436	196	982
GJ4	21.6102	72.2693	Alluvium	Pump	7.41	2,900	693	1.72	0.01	0.37	5,790	438	3,503	12,807	694	1,804
GJ5	21.0591	71.7591	Alluvium	Pump	6.86	1,960	414	2.52	0.12	0.30	6,982	75	1,861	7,149	1,158	1,068
GJ6	20.7613	71.0551	Limestone	Pump	7.23	8,770	427	1.69	0.06	1.28	50,778	1,548	18,888	60,067	85	17,487
GJ7	20.8979	70.3932	Limestone	Borewell	7.10	2,210	714	0.35	0.01	4.00	7,790	1,416	1,966	14,782	572	876
GJ8	21.6439	69.6032	Limestone	Borewell	7.04	1,430	329	0.88	0.10	3.45	6,016	1,566	869	5,044	23	511
GJ9	22.2399	68.9323	Alluvium	Pump	7.32	4,750	443	0.62	0.20	0.31	30,717	3,077	3,518	32,952	1,634	2,310
GJ10	22.4717	70.0786	Basalt	Pump	7.29	1,040	738	0.50	0.18	1.36	4,831	416	799	2,598	1,222	412
AP1	18.9408	84.5648	Gneiss	Pump	7.26	983	1,144	0.59	0.02	2.33	2,843	1,146	746	2,877	870	391
AP3	17.3167	82.5695	Gneiss	Pump	6.47	730	516	1.93	0.21	1.01	2,307	145	511	3,496	9	530
AP4	16.9569	82.2552	Alluvium	Pump	7.02	1,140	690	0.48	0.08	1.05	4,187	149	1,031	4,641	36	338
AP5	16.3966	81.8095	Alluvium	Borewell	6.90	260	274	1.68	0.15	1.13	844	59	395	566	32	129
AP6	16.1777	81.1385	Alluvium	Pump	7.33	5,310	150				32,830	1,509	9,561	30,229	17	4,950
AP7	15.7809	80.3801	Alluvium	Borewell	7.79	6,920	381	0.38	0.13	1.21	64,200	1,076	1,545	53,965	189	1,501
AP8	15.5046	80.0365	Alluvium	Hand pump	7.28	6,010	578	0.94	0.07	0.70	29,491	7,375	4,783	43,049	6,876	3,271
AP9	14.2971	80.0904	Alluvium	Pump	7.55	2,100	837	3.14	0.29	0.24	29,426	265	83	7,561	1,407	1,917
AP10	13.5888	80.0343	Laterite	Pump	7.07	1,500	629	0.69	0.01	0.58	9,224	315	1,236	6,960	1,175	2,184
GA1	14.9111	74.0816	Granite	Hand pump	6.65	460	523	1.1	0.0	0.55	806	72	750	1,027	54	112
GA2	14.9592	74.0551	Granite	Hand pump	6.66	4,480	246	1.2	0.0	0.52	29,870	218	3,038	43,312	59	1,176
GA3	15.0021	74.0786	Granite	Borewell	5.75	130	218	0.6	0.2	0.57	627	43	84	642	95	17
GA4	15.0421	73.9991	Granite	Hand pump	5.37	150	266	1.1	0.1	0.62	645	76	135	754	155	64
GA5	15.1261	73.9495	Gneiss	Borewell	5.98	182	86	0.6	0.1		304	91	170	322	6	13
GA6	15.2068	73.9504	Gneiss	Hand pump	6.41	430	91	0.5	0.1	1.62	1,248	106	260	733	154	308
GA7	15.7103	73.7257	Laterite	Borewell	6.37	1,541	209	0.7	0.2	0.87	7,319	127	1,860	14,613	21	584
KA1	12.7884	74.8593	Gneiss	Pump	5.05	520	168	0.3	0.1	1.25	2,671	321	341	2,962	1,429	38
KA2	12.8748	74.8292	Gneiss	Pump	5.98	260	291	1.0	0.1	0.50	843	470	142	590	306	288
KA3	13.2228	74.7845	Gneiss	Pump	5.60	310	158	−0.2	0.0	4.06	664	107	240	464	941	234
KA4	13.3889	74.7431	Gneiss	Pump	5.33	150	233	1.3	0.1	0.94	556	30	61	592	129	14
KA5	13.6189	74.6926	Alluvium	Pump	6.71	510	147	0.1	0.1		1,535	476	244	1,656	728	242
KA6	13.8183	74.6343	Gneiss	Pump	5.62	190	128	−0.1	0.1	1.17	618	15	107	897	241	102
KA7	14.0271	74.5291	Laterite	Borewell	4.79	170	87	0.8	0.2	2.08	817	166	75	1,212	138	32
KA8	14.2417	74.4468	Laterite	Pump	6.10	190	779	0.9	0.1	1.72	356	79	516	256	2	23
KA9	14.4308	74.4231	Alluvium	Pump	5.83	99	171	1.4	0.1	0.88	375	54	91	343	9	35
KA10	14.6572	74.3121	Laterite	Pump	6.65	970	190	1.4	0.1	1.11	3,394	141	1,163	6,326	421	560
KL1	8.3945	77.0885	Gneiss	Pump	6.02	334	140	−0.01	0.05	1.65	1,448	275	152	1,701	383	239
KL2	8.8634	76.6935	Gneiss	Pump	5.63	150	199	0.11	0.14		685	70	66	695	150	61
KL3	9.3183	76.4217	Alluvium	Pump	5.67	478	314	1.25	0.05	0.64	2,100	205	541	2,277	20	579
KL4	9.9994	76.2929	Alluvium	Pump	5.96	92	119	1.04	0.10	1.26	291	87	72	365	7	40
KL5	10.4192	76.1052	Alluvium	Borewell	7.05	480	337	−0.43	0.04	2.90	730	373	186	683	259	312

19449224, 2025, 8, Downloaded from https://agupubs.onlinelibrary.wiley.com/doi/10.1029/2025GB008706 by Cochrane France, Wiley Online Library on [22/09/2025]. See the Terms and Conditions (https://onlinelibrary.wiley.com/terms-and-conditions) on Wiley Online Library for rules of use; OA articles are governed by the applicable Creative Commons License

Table 1
Continued

	Latitude	Longitude	Aquifer lithology	Type	pH	Conductivity µS/cm	DSi µM	δ^{30}Si ‰	1SD	Ge/Si µmol/mol	Na µM	K µM	Mg µM	Cl µM	NO3 µM	SO4 µM
KL6	10.9248	75.9139	Alluvium	Pump	6.15	150	78	0.57	0.07	1.75	478	70	64	404	29	250
KL7	11.4696	75.6548	Alluvium	Borewell	5.88	140	136	−0.10	0.10	3.82	236	90	50	411	28	82
KL8	11.8847	75.3725	Laterite	Pump	6.33	180	170	1.29	0.07	1.15	665	146	147	802	423	155
KL9	12.2428	75.1449	Alluvium	Pump	6.42	260	180	0.38	0.24	1.09	908	143	175	834	104	287
KL10	12.6821	74.9032	Alluvium	Pump	5.63	140	204	0.42	0.28	0.80	610	51	74	655	1	37
MH1	15.7243	73.6882	Schist	Hand pump	6.32	200	94	0.68	0.02	2.03	376	66	80	518	14	50
MH2	16.1077	73.4725	Quartzite	Pump	5.60	1,457	527	0.18	0.04	2.16	259	39	581	308	22	9,713
MH3	16.4731	73.3943	Basalt	Pump	4.87	200	445	0.63	0.17	0.99	309	17	103	409	36	32
MH4	16.9938	73.317	Laterite	Pump	6.22	280	100	0.52	0.09	4.10	706	85	155	747	203	261
MH5	17.5015	73.1855	Laterite	Pump	5.96	160	236	1.00	0.06	0.76	372	0	143	372	4	39
MH6	17.9758	73.0918	Basalt	Borewell	6.27	230	813	0.66	0.02	0.45	732	166	311	553	227	51
MH7	18.6471	72.8783	Basalt	Hand pump	7.33	2,270	520	0.99	0.00	0.28	21,078	253	1,759	17,624	14	1,828
MH8	19.3753	72.8275	Alluvium	Pump	7.14	1,250	884	0.86	0.05	0.17	7,363	210	1,278	4,439	74	582
MH9	19.9562	72.8231	Basalt	Pump	6.82	410	1,246	1.26	0.11	0.58	690	41	852	388	7	99
MH10	20.1356	72.8065	Basalt	Pump	6.79	560	1,070	1.05	0.06	0.79	1,053	0	769	892	32	188
OD1	21.6701	87.2859	Alluvium	Borewell	7.26	840	983	−0.15	0.09	1.02	3,386	96	758	259	31	135
OD2	21.3413	86.7631	Alluvium	Borewell	7.03	570	752	−0.04	0.19	2.68	1,657	31	872	743	64	57
OD3	20.8119	86.7609	Alluvium	Pump	7.25	1,030	565	−1.07	0.10	3.25	5,726	155	913	3,947	60	316
OD4	20.5014	86.3277	Alluvium	Pump	7.16	715	407	−0.55	0.08	0.82	4,190	242	570	2,831	4	78
OD5	20.0989	86.1886	Alluvium	Pump	6.17	650	687	0.47	0.14	1.46	2,966	271	575	2,347	6	218
OD6	19.8422	85.9032	Alluvium	Borewell	6.85	830	460	0.40	0.20	2.07	2,750	202	903	2,504	10	135
OD7	19.9016	85.3656	Laterite	Pump	6.29	240	963	0.12	0.01	2.31	770	139	171	364	60	44
OD8	19.5972	85.1211	Alluvium	Pump	6.37	665	1,354	0.54	0.10	0.83	1,434	654	608	2,935	446	212
OD9	19.3503	84.9882	Alluvium	Borewell	7.07	876	350	0.82	0.11	0.76	4,398	44	1,310	3,783	3	1,058
OD10	19.1611	84.7112	Alluvium	Hand pump	6.89	5,830	680	0.72	0.27	1.19	20,426	12,808	7,858	37,207	2,564	4,963
TN1	12.9399	80.2401	Alluvium	Pump	7.16	5,420	440	0.74	0.2	1.12	34,904	892	5,186	40,760	65	4,926
TN2	12.3821	80.0894	Alluvium	Pump	6.31	280	319	1.32	0.1	0.73	793	61	401	1,082	245	157
TN3	11.7479	79.7687	Alluvium	Pump	6.85	2,090	775	1.88	0.1	0.13	9,890	832	2,143	9,685	8	1,937
TN4	11.0311	79.8503	Alluvium	Borewell	7.25	2,280	292	1.50	0.2	0.88	14,810	1,073	1,740	14,114	28	1,927
TN5	10.3765	79.8497	Alluvium	Pump	7.15	2,750	670	1.19	0.0	0.54	10,826	2,765	2,499	11,656	5,196	2,049
TN6	10.0388	79.2333	Alluvium	Pump	7.09	810	382	0.65	0.0	1.26	3,629	194	623	3,694	775	425
TN7	9.3316	78.9741	Alluvium	Hand pump	7.20	1,370	509	0.70	0.1	0.57	7,161	213	865	6,412	584	520
TN8	9.2353	78.7875	Alluvium	Pump	7.36	5,820	590	4.29	0.1	0.08	40,161	4,712	3,510	41,994	3,599	4,000
TN9	8.7571	78.1566	Alluvium	Borewell	7.10	1,100	837	3.26	0.0		2,903	1,931	1,995	2,503	4	1,080
TN10	8.0885	77.5493	Alluvium	Hand pump	7.08	1,760	1,072	0.94	0.0	0.40	8,684	795	1,095	11,872	2,632	882
WB1	22.1889	88.7132	Alluvium	Pump	7.30	1,042	422	−0.66	0.17	0.00	8,752	155	498	2,087	119	305
WB2	22.2271	88.4461	Alluvium	Pump	7.31	1,100	473	−0.51	0.05	2.36	6,603	167	1,262	2,828	42	784
WB3	22.2181	88.0949	Alluvium	Pump	7.21	1,250	738	−0.49	0.06	0.66	5,943	102	854	3,885	24	544
WB4	22.4632	87.9733	Alluvium	Pump	7.03	1,350	830	−0.37	0.02	1.28	9,000	156	677	5,635	7	243
WB5	22.0428	88.0657	Alluvium	Borewell	7.49	1,600	602	−0.35	0.05	1.72	9,318	83	1,053	9,841	14	351
WB6	22.0129	87.8173	Alluvium	Pump	7.12	1,500	711	−0.21	0.15	1.68	6,256	131	1,628	7,573	41	482

19449224, 2025, 8, Downloaded from https://agupubs.onlinelibrary.wiley.com/doi/10.1029/2025GB008706 by Cochrane France, Wiley Online Library on [22/09/2025]. See the Terms and Conditions (https://onlinelibrary.wiley.com/terms-and-conditions) on Wiley Online Library for rules of use; OA articles are governed by the applicable Creative Commons License

Table 1
Continued

	Latitude	Longitude	Aquifer lithology	Type	pH	Conductivity µS/cm	DSi µM	δ^{30}Si ‰	1SD	Ge/Si µmol/mol	Na µM	K µM	Mg µM	Cl µM	NO3 µM	SO4 µM
WB7	21.8712	87.7571	Alluvium	Pump	7.03	1,647	639	−0.31	0.14	2.81	6,777	162	2,810	12,548	18	423
WB8	21.7852	87.7441	Alluvium	Pump	7.35	3,680	290	4.48	0.02	0.18	26,622	1,203	3,093	20,186	129	3,993
WB9	21.7205	87.6637	Alluvium	Pump	6.91	610	1,085	−0.84	0.10	0.31	3,005	114	1,077	2,247	7	101
WB10	21.6234	87.5206	Laterite	Borewell	7.26	923	365	1.59	0.02	0.61	4,364	338	2,044	2,931	164	1,182

precipitated brucite. After centrifugation and recovery of the precipitate, the supernatant from the first step was again subjected to a second addition of 1% NaOH, and the additional precipitate was recovered by centrifugation after 1–2 hr. Both brucite precipitates were dissolved with 1M HCl and merged. The DSi concentration of the supernatant was analyzed by spectrophotometer and found negligible (on average <2% of initial Si), confirming that all the Si was adsorbed onto the brucite precipitate.

Separation of Si from other cations was carried out using cation exchange resin (BioRad DOWEX 50W-X12, 200–400 mesh, in H^+ form) following the procedure of Georg et al. (2006a). After the purification process, an aliquot was analyzed for determining the concentration of major elements (Na, Mg, Ca, K, DSi) by ICP-MS (Agilent 7500a) to ensure that the Si/X (Where X = Na, K, Ca or Mg) weight ratio was always >50 to minimize the matrix effects in the plasma. The organic matrix was removed by treatment with 50 µL of 30% H_2O_2 since it has been shown to potentially induce a matrix bias during MC-ICP-MS analyses (Hughes et al., 2011). The remaining potential matrix effect from Cl^-, NO^-_3 and SO_4^{2-} was corrected by the artificial doping of anions (Merck, Suprapur grade H_2SO_4, HNO_3 and HCl) in all samples and standards (Hughes et al., 2011). The measurements were performed on MC-ICP-MS (Thermo Neptune+, LSCE-IPSL, Gif-sur-Yvette) in dry plasma mode with Mg doping, as described by Closset et al. (2016). Samples were injected into the plasma with an ApexΩ HF desolvating nebulization system connected with a PFA nebulizer (100 µL/min uptake rate). The δ^{30}Si values were expressed as the permil deviation of the ^{30}Si/^{28}Si ratio from the quartz standard NBS28 (RM8546), expressed as

$$\delta^{30}\text{Si}_{\text{sample}} = \left[\left({}^{30}\text{Si}/{}^{28}\text{Si}\right)_{\text{sample}}/\left({}^{30}\text{Si}/{}^{28}\text{Si}\right)_{\text{NBS28}} - 1\right] * 1000 \tag{1}$$

Blank levels were below 1% of the main signal and were subtracted from each sample and standard analysis. The analysis was carried out in medium-resolution mode (m/Δm ~ 6,000) to optimize the separation of the ^{30}Si peak and $^{14}N^{16}O$ interference and was performed on the interference-free left side of the flat peak (Abraham et al., 2008). The δ^{29}Si and δ^{30}Si values were compared to the mass-dependent fractionation line, and samples falling outside of its analytical error were excluded from the final data set (Figure S1 in Supporting Information S1). Typical analytical conditions are provided in Table S1 of Supporting Information S1. Laboratory protocol has been intercalibrated for seawater as part of the GEOTRACES intercalibration exercise generated over the entire procedure (Grasse et al., 2017). The analytical precision and accuracy were monitored by the long-term measurements of a secondary reference material, Diatomite, whose average δ^{30}Si value of 1.19 ± 0.18‰ (2SD, $n = 100$) was in agreement with the intercalibration of 1.26 ± 0.2‰ (Reynolds et al., 2007). All the samples measured in the present study are chemically replicated at least once and 12 samples were chemically triplicated with an average 2SD of ±0.19 ‰.

2.5. Germanium Analysis

The Ge concentrations in groundwater samples were measured by isotope dilution using a ^{73}Ge spike (Neonest AB®) added to approximately 10 ml of samples before a two-step pre-concentration procedure adapted according to the MAGIC co-precipitation technique (Karl & Tien, 1992; Reynolds, 2006). The Ge separation and purification were achieved using the BioRad cation exchange resin DOWEX 50W-X12 (200–400 mesh). The analyses were performed on a high-resolution inductively coupled double-focusing plasma mass spectrometer (Element XR, Thermo Fischer Scientific®) at Géosciences Environnement Toulouse (Toulouse, France). To improve the

19449224, 2025, 8, Downloaded from https://agupubs.onlinelibrary.wiley.com/doi/10.1029/2025GB008706 by Cochrane France, Wiley Online Library on [22/09/2025]. See the Terms and Conditions (https://onlinelibrary.wiley.com/terms-and-conditions) on Wiley Online Library for rules of use; OA articles are governed by the applicable Creative Commons License

19449224, 2025, 8, Downloaded from https://agupubs.onlinelibrary.wiley.com/doi/10.1029/2025GB008706 by Cochrane France, Wiley Online Library on [22/09/2025]. See the Terms and Conditions (https://onlinelibrary.wiley.com/terms-and-conditions) on Wiley Online Library for rules of use; OA articles are governed by the applicable Creative Commons License

sensitivity of the analyses and to reduce the matrix interferences, a CETAC Aridus II desolvating nebulizer has been coupled to the HR-ICP-MS. A bracketing standard was run for every five samples to correct for the instrumental drift during the analysis. All procedure blanks analyzed were on average <0.02 nM ($n = 4$), and were subtracted from each sample. The signal intensity measured for the ^{72}Ge and ^{73}Ge isotopes in the samples were respectively 40 and 50 times higher compared to the limit detection of the instrument. The Ge concentration in selected supernatant solutions ($n = 14$) after MAGIC co-precipitation were below detection limit of the instrument, ensuring complete Ge recovery. The accuracy of Ge measurement were determined by repeated analyses of the reference material SLRS-6 (NRC-Canada), giving Ge concentration of 0.088 ± 0.016 nM (2SD, $n = 5$). This was in accordance with published values measured by HR-ICP-MS (Yeghicheyan et al., 2019, [Ge] = 0.094 ± 0.010 nM, $n = 15$) and with unpublished values analyzed by isotope dilution using a ^{70}Ge spike at GET (0.090 ± 0.002 nM, $n = 4$).

2.6. Modeling Si Isotopic Evolution in Groundwater

Once solubilized by the silicate mineral weathering reactions, the DSi is partitioned into secondary clays, taken up by plants and/or adsorbed onto Fe oxy-hydroxides. Depending on the nature and the intensity of the partitioning processes, the isotopic signature of DSi will evolve between two theoretical frameworks: (a) a Rayleigh model, where precipitated solids, adsorbed phase, or taken-up fraction do not further exchange with the remaining solution (Equation 2), (b) a steady-state open flow through batch reactor model (here onwards steady-state model) where supply of fresh Si into the system is balanced by precipitation and/or uptake and/or adsorption (Equation 3) (Bouchez et al., 2013; Frings et al., 2015).

$$\textbf{Rayleigh :}\ \delta^{30}\mathrm{Si}_{\mathrm{GW}} = \delta^{30}\mathrm{Si}_{\mathrm{o}} + {}^{30}\varepsilon * \ln\left(f_{Si}\right) \tag{2}$$

$$\textbf{Steady state :}\ \delta^{30}\mathrm{Si}_{\mathrm{GW}} = \delta^{30}\mathrm{Si}_{\mathrm{o}} - {}^{30}\varepsilon * \left(1 - f_{Si}\right) \tag{3}$$

The $\delta^{30}\mathrm{Si}_{\mathrm{GW}}$ value denotes the measured δ^{30}Si values of groundwater, and $\delta^{30}\mathrm{Si}_{\mathrm{o}}$ denotes the initial δ^{30}Si, which is the upper continental crust (UCC) composition of −0.25 ± 0.16‰ (Savage et al., 2013). The published δ^{30}Si values of granitic gneiss (−0.3 ± 0.1‰, Riotte, Meunier, et al., 2018) and Deccan basalts (−0.1 ± 0.1‰ Wille et al., 2018) in Indian subcontinent confirms the narrow δ^{30}Si variability in bedrock composition. The quantity $^{30}\varepsilon$, also known as isotope fractionation, is defined as $^{30}\varepsilon = \alpha\text{-}1$ and expressed in per mil (‰) (Coplen, 2011). Here α is the isotopic fractionation factor associated with secondary mineral precipitation, adsorption or plant uptake. The f_{Si} in Equations 2 and 3 indicates the fraction of Si remaining in the dissolved phase, estimated by normalizing it with a conservative element (in our case Na) in solution and bedrock and estimated as:

$$f_{\mathrm{Si}} = \left(\mathrm{DSi}/\mathrm{Na}^{*}\right)_{\mathrm{groundwater}}/\left(\mathrm{Si}/\mathrm{Na}\right)_{\mathrm{UCC}} \tag{4}$$

We assume the stoichiometric release of Si and Na from the bedrock as a result of silicate weathering and preferential loss of Si from solution by incorporation into secondary phases (Georg et al., 2006b; Hughes et al., 2013; Wedepohl, 1995), while Na is only marginally incorporated and remains in solution. The f_{Si} values reflect the proportion of Si incorporated into the secondary phases. A value of 0 implies complete removal, whereas a value of 1 indicates that Si remains entirely in solution. The "*" denotes the atmospheric/seawater correction to discard any contribution from atmospheric deposits and seawater mixing using Cl concentration as described in Gaillardet et al. (1999);

$$[\mathrm{Na}^{*}] = [\mathrm{Na}]_{\mathrm{measured}} - (\mathrm{Na}/\mathrm{Cl})_{\mathrm{rain}} * [\mathrm{Cl}]_{\mathrm{measured}} \tag{5}$$

here $(\mathrm{Na/Cl})_{\mathrm{rain}}$ is the elemental seawater ratio and $[\mathrm{Na}]_{\mathrm{measured}}$ and $[\mathrm{Cl}]_{\mathrm{measured}}$ are measured concentration in groundwater (Mondal et al., 2011). Further interpretation relies on two assumptions: (a) isotopic fractionation during mineral dissolution is considered transient and negligible as weathering progresses over time, (b) the UCC elemental and δ^{30}Si signature is considered as a reasonable approximation for the signature of primary silicates (Frings, Oelze, et al., 2021; Geilert et al., 2014; Ziegler et al., 2005). However, the calculated f_{Si} values are likely to be an overestimate, given that quartz correction has not been applied for the UCC composition.

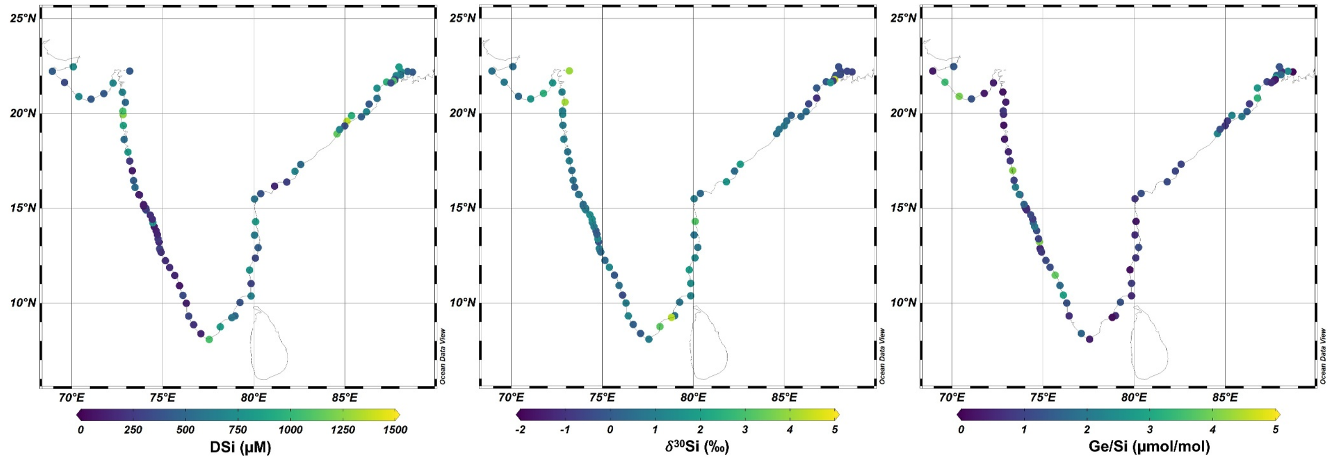

Figure 1. The schematic map of the Indian subcontinent shows the sampling location of 86 coastal groundwater samples and the dissolved silicon (DSi, μM), δ^{30}Si (‰), and Ge/Si (μmol/mol) ranges.

3. Results

3.1. Coastal Groundwater Chemical Composition

The sampling details of elemental and isotopic composition are given in Table 1. The electrical conductivity (EC) of coastal groundwater samples ranged from 92 to 8,770 μS/cm, and an average pH was 6.7 ± 0.7 (Figure S2 in Supporting Information S1). High conductivity can be indicative of seawater intrusion, high evapotranspiration and/or excessive contribution from fertilizers. We identified 10 coastal groundwaters in India with EC > 3,000 μS/cm and Cl concentration >20 mM that can be considered as brackish groundwater (Jiao & Post, 2019). The fraction of seawater in groundwater was estimated using two endmember mixing based on Cl concentration: (a) coastal Bay of Bengal seawater as saline endmember (Jiao & Post, 2019; Mondal et al., 2011) and (b) average fresh groundwater from the present study as fresh endmember. The estimated fraction of seawater in coastal groundwater ranges from 3% to 10%. Based on the measured elemental concentration, Na was identified as the dominant cation in coastal groundwater for most samples, followed by Mg, K and Ca. The atmospheric correction was not applicable in few groundwater as a result of significant Cl contribution from fertilizers, such as potash (KCl), which would significantly overcorrect the Na concentration (Buvaneshwari et al., 2020). The concentration of anions in groundwater follows the order $[\mathrm{Cl}^-] > [\mathrm{SO_4}^{2-}] > [\mathrm{NO_3}^-]$ (Table 1).

3.2. Dissolved Silicon and Silicon Isotopes

The dissolved silicon (DSi) concentration in coastal groundwater samples exhibits large spatial variability, ranging from 78 to 1,354 μM, with an average of 484 ± 304 μM (±1SD, $n = 86$). The groundwater DSi values were comparable to reported global coastal fresh groundwater DSi values from extrusive igneous (604 ± 192 μM) and complex lithologies (288 ± 245 μM) (Rahman et al., 2019). The δ^{30}Si values of coastal groundwater ranged from −1.1 to 4.5‰, with an average composition of 0.8 ± 1.1‰ ($n = 85$, ±1SD), close to the reported global δ^{30}Si value of groundwater (0.8 ± 0.8‰, $n = 117$; Frings et al., 2016, Ehlert, Reckhardt, et al., 2016; Ehlert, Doering, et al., 2016; Martin et al., 2021, Kavil et al., 2024) and more heterogenous (Figure 2). The Indian coastal groundwater also exhibits higher DSi compared to Indian rivers (176 ± 101 μM, ±1SD, $n = 168$) and lower δ^{30}Si values (1.5 ± 0.6‰,±1SD, $n = 152$) (Ganges: Fontorbe et al., 2013; Frings et al., 2015; Cauvery and Netravathi: Sarath et al., 2022). Overall, a low groundwater DSi was observed in the West coast of India (365 ± 280 μM, ±1SD, $n = 47$) compared to the East (627 ± 271 μM, ±1SD, $n = 39$) (Figure 1). However, there was no significant difference in δ^{30}Si between the east and west coast. The heaviest and lightest δ^{30}Si values were observed in alluvial aquifers located on the North East coast of India. We do not observe any consistent relationship between the DSi and δ^{30}Si values in Indian coastal groundwater and within similar lithology or climatic zones (Figure 2).

19449224, 2025, 8, Downloaded from https://agupubs.onlinelibrary.wiley.com/doi/10.1029/2025GB008706 by Cochrane France, Wiley Online Library on [22/09/2025]. See the Terms and Conditions (https://onlinelibrary.wiley.com/terms-and-conditions) on Wiley Online Library for rules of use; OA articles are governed by the applicable Creative Commons License

19449224, 2025, 8, Downloaded from https://agupubs.onlinelibrary.wiley.com/doi/10.1029/2025GB008706 by Cochrane France, Wiley Online Library on [22/09/2025]. See the Terms and Conditions (https://onlinelibrary.wiley.com/terms-and-conditions) on Wiley Online Library for rules of use; OA articles are governed by the applicable Creative Commons License

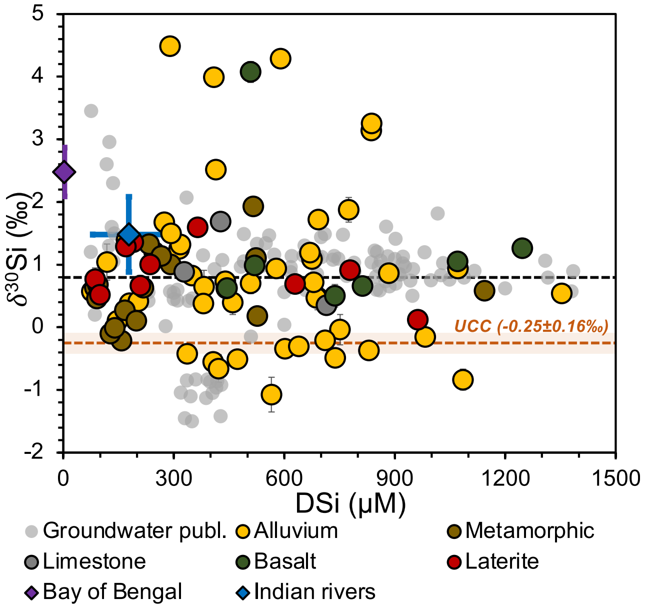

Figure 2. Plot of δ^{30}Si versus DSi (μM) in coastal groundwater of India sorted by aquifer lithology. The compiled average (±1SD) of DSi and δ^{30}Si from Indian river water (Fontorbe et al., 2013; Frings et al., 2015, 2016; Sarath et al., 2022) and the surface Bay of Bengal seawater (Singh et al., 2015) are given as blue and purple diamond respectively. The brown line and shaded area represent the upper continental crust δ^{30}Si composition and ±1SD published by Savage et al. (2013) and the black line represents the global groundwater average reported so far (0.8 ± 0.8‰, see Section 3.2 for references).

3.3. Germanium Concentration and Ge/Si Ratio

The germanium concentration in coastal groundwater ranged from 0.04 to 2.9 nM, with an average of 0.57 ± 0.6 nM ($n = 80$, 1SD). The measured Ge values fall in the higher range of reported Ge concentration in groundwater globally, ranging from 0.03 to 0.5 nM (Aguirre et al., 2017; Baronas et al., 2020). The Ge/Si ratio in Indian coastal groundwater ranged from 0.1 to 4.1 μmol/mol, with an average of 1.3 ± 1.0 μmol/mol, higher than the current published average of 0.4 ± 0.4 nM ($n = 50$, Aguirre et al., 2017; Baronas et al., 2020). We observe no consistent relationship between Ge/Si and regional lithology and mean annual rainfall. The lowest Ge/Si values were observed in alluvial groundwaters from the South East coast and highest in the lateritic groundwater on the East coast.

4. Discussion

Unlike river systems, which integrate water-soil-plant interactions at the scale of the entire river basin, aquifers are spatially limited, reflecting weathering and biogeochemical processes within the local critical zone. A systematic groundwater sampling along the Indian coast, spanning diverse pedoclimatic contexts within the peninsula allows us to discuss the potential broad environmental controls on coastal groundwater δ^{30}Si (e.g., lithology, climate; see Section 4.1) and also the sources and processes controlling the Si isotopic composition in the groundwater (weathering, adsorption, plant uptake; Section 4.2). Finally, we quantify Si fluxes and isotopic impact of fresh and saline SGD along the Indian coast (Section 4.3).

4.1. Broad Environmental Controls on Groundwater δ^{30}Si

Over longer timescales, the lithology and climate are two major factors determining the silicate weathering rates of a region (Maher, 2010; White & Blum, 1995). We do not observe any significant difference in δ^{30}Si of coastal groundwater from the major aquifer lithologies on the Indian coast (Figure 3). This indicates that the aquifer lithology has no impact on the partitioning of silicon during the water-rock-plant interactions within the critical zone. The high DSi in groundwater from basaltic aquifers in west coast can be explained by intrinsically high reactivity of basaltic mafic minerals (Dessert et al., 2003), but limited groundwater samples are available from basaltic and granitic lithologies compared to alluvium (Table 1). Another interesting observation from Figure 3 is the highly heterogenous DSi (531 ± 284 μM) and δ^{30}Si (0.84 ± 1.3‰, $n = 48$) signatures in alluvial aquifers, which includes all groundwater lower than the UCC composition as well as most of the highest δ^{30}Si signatures. The findings also complement the previously observed 2‰ range in groundwater δ^{30}Si measurements within sedimentary aquifer types, such as sandstone, limestone and alluvium from various regions around the globe (Georg, West, et al., 2009, Georg, Zhu, et al., 2009; Martin et al., 2021). The alluvium aquifer systems cover almost 30% of India, and the Quaternary alluvium can extend up to hundreds of meters deep along the coast particularly in the Ganga-Brahmaputra delta (CGWB, 2012). The alluvial sediments primarily consist of detrital quartz, feldspar grains and clay minerals, including kaolinite and illite (Mukherjee et al., 2009). The unconsolidated alluvial aquifers exhibit high groundwater recharge rates, primarily due to high permeability and transmissivity compared to fractured-crystalline aquifers and intense groundwater abstraction and return flow cycles related to agriculture (Bhanja et al., 2019). This, along with high horizontal hydraulic conductivity (10–800 m/day) can result in mixing with surface water and runoff components through highly porous and permeable sands and gravel (Bhanja et al., 2019; Larkin & Sharp, 1992). The mixing of Si reservoirs with distinct δ^{30}Si values, each driven by biogeochemical processes within the weathering zone (for e.g. plant uptake or clay dissolution), is required to explain such large variability in δ^{30}Si values of alluvial groundwater (Georg, West, et al., 2009; Georg, Zhu, et al., 2009; Kavil et al., 2024).

The groundwater recharge dynamics in India largely depend on the balance between annual monsoonal precipitation and pumping for irrigated agriculture and domestic needs, which has also led to rapid groundwater depletion in the Indian Peninsula (Asoka et al., 2017; Rodell et al., 2009). Interestingly, the δ^{30}Si and DSi

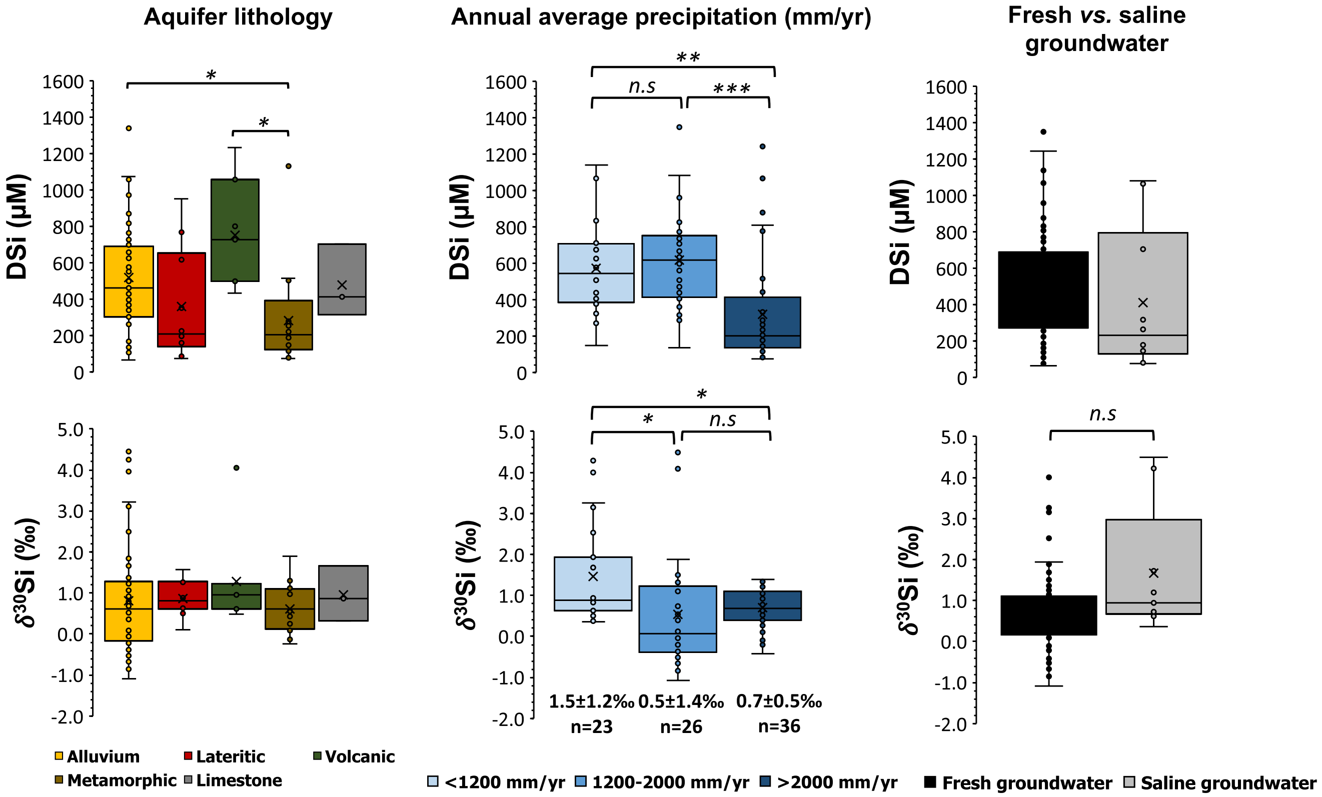

Figure 3. Box plot showing DSi and of δ^{30}Si of Indian coastal groundwater according to the type of lithology, the annual average precipitation and seawater intrusion in groundwater. The aquifer lithology classification is based on WRIS, India and precipitation data from AQUASTAT, FAO and saline intrusion based on Cl concentration and conductivity. The bracket represents the categories with significant differences, and significance is based on ANOVA and Games-Howell post hoc test and is the level of significance is denoted by * (p-value < 0.05), ** (p-value < 0.01), *** (p-value < 0.001) and (n.s. Denotes no significance).

composition of coastal groundwater in regions with low annual average rainfall (<1,200 mm yr^{-1}) was significantly higher than the higher rainfall settings (Figure 3). The rainfall intensity of the region can directly impact the δ^{30}Si composition of groundwater by controlling the weathering rates and nature of secondary phases formed within the weathering zone (Opfergelt et al., 2012). Here, we limit our discussion to the long-term impact of regional rainfall on groundwater silicon cycling and not seasonal variability. The high annual rainfall leads to intense chemical weathering and formation of kaolinites and iron-aluminum oxy-hydroxides, which are predominant in the soil profiles on the West Coast, while the low rainfall regions of the East Coast are dominated by smectite-type clays (Deepthy & Balakrishnan, 2005). The published evidence suggests that the δ^{30}Si value of kaolinite-type clays is more fractionated in Si isotopes with respect to parent bedrock than in smectite-type clays (Cornelis et al., 2019; Opfergelt et al., 2012). Assuming a similar proportion of Si immobilized as clays, the residual solution (such as soil solutions and groundwater) from soil profiles with high rainfall (i.e., kaolinite dominant soil profiles) should exhibit a heavier δ^{30}Si composition. However, we observe the contrary in coastal groundwater, and thus, differences in weathering intensity and clay formation cannot explain the observed heavy isotopic composition in groundwater from low rainfall settings. In addition to direct control of the formation of secondary phases, rainfall can also indirectly affect the water use dynamics of the region. The coastal plains are cultivation hotspots for high-water demand crops such as rice, maize and sugarcane, which can take up dissolved silicon from irrigated water (FAO, 2022; Haynes, 2017; Sarath et al., 2022). Thus, indirect groundwater recharge as agricultural return flow into the aquifers can alter the Si cycling in groundwater in areas under irrigated agriculture (Dewandel et al., 2008; Sarath et al., 2022). In low rainfall and arid climate settings, the irrigation return flow can significantly increase the groundwater DSi and EC as a result of evapotranspiration, and $\mathrm{NO_3}^-$ is typically derived from fertilizers (Figure S3 in Supporting Information S1). A detailed discussion of the impact of plant uptake in groundwater δ^{30}Si is given in Section 4.2.2.

19449224, 2025, 8, Downloaded from https://agupubs.onlinelibrary.wiley.com/doi/10.1029/2025GB008706 by Cochrane France, Wiley Online Library on [22/09/2025]. See the Terms and Conditions (https://onlinelibrary.wiley.com/terms-and-conditions) on Wiley Online Library for rules of use; OA articles are governed by the applicable Creative Commons License

19449224, 2025, 8, Downloaded from https://agupubs.onlinelibrary.wiley.com/doi/10.1029/2025GB008706 by Cochrane France, Wiley Online Library on [22/09/2025]. See the Terms and Conditions (https://onlinelibrary.wiley.com/terms-and-conditions) on Wiley Online Library for rules of use; OA articles are governed by the applicable Creative Commons License

The Si in coastal aquifers can also originate from seawater intrusion, where the local seawater from the Bay of Bengal exhibits a low DSi (<60 μM) and high δ^{30}Si values (2.1 ± 0.5‰) (Singh et al., 2015). The identified brackish groundwater along the Indian coast spanned alluvial, granitic and limestone aquifer lithologies, with varying degrees of seawater mixing (3%–10%) and shows no relationship with DSi (Figure 3, Figure S4 in Supporting Information S1). The brackish groundwater exhibits variable DSi (from 150 to 680 μM) and δ^{30}Si values (0.4–4.5‰), and a non-conservative mixing trend with significantly high δ^{30}Si composition (Figure S4 in Supporting Information S1). The non-conservative nature of mixing makes it difficult to constrain a saline SGD endmember based on brackish groundwater, and to use DSi as a tracer for SGD in Indian coast (Oehler et al., 2019). The aquifer sediments in alluvial plains can host reactive silicates as well as recent diatomaceous earth, which can alter the DSi signatures in mixing zones (De & Bhattacharyya, 2009; Oehler et al., 2019). However, high δ^{30}Si values in brackish groundwaters TN8 and WB8 are unlikely to result from biogenic silica (diatoms) dissolution, as δ^{30}Si values of these Si sources are typically lower than the seawater composition (Ehlert, Doering, et al., 2016; Savage et al., 2013). Thus, the influence of seawater intrusion on the Si isotopic composition of coastal groundwater is considered to be negligible. Overall, our results highlight the large variability in DSi and δ^{30}Si composition of alluvial groundwater, with a significantly heavy δ^{30}Si composition in coastal groundwater with low annual rainfall. The lithology and climate are not the primary drivers of silicon isotopic signatures in Indian coastal groundwaters. In the next section, we will look more closely into specific sources and processes that can explain the observed δ^{30}Si composition in coastal groundwater.

4.2. Si Sources and Biogeochemical Processes in Coastal Groundwater

4.2.1. Incongruent Silicate Weathering Signatures in Groundwater

The primary source of dissolved silicon in groundwater is the weathering of silicate minerals, which can be partly immobilized in soil and saprolite through biogeochemical processes before reaching the saturated zone (Georg, West, et al., 2009; Pogge von Strandmann et al., 2014). Indeed, most of the groundwater samples exhibit heavier δ^{30}Si than the UCC signature of −0.25 ± 0.16‰ and broadly correlates negatively with the Ge/Si ratio (Figure 4, $R^2 = 0.24$, $p\ value < 0.01$), evidencing incongruent nature of silicate weathering with the formation of secondary phases (Baronas et al., 2020; Savage et al., 2013). The extent of partitioning into secondary phases, estimated as f_{Si} (Equation 4), indicates that 80% to >99% of Si mobilized by silicate weathering was incorporated into secondary phases. The resulting δ^{30}Si composition of the DSi fraction reaching coastal groundwater systems can be modeled based on the extent of incorporation and/or adsorption onto secondary mineral phases (clays and/or oxy-hydroxides) and, plant uptake of DSi in shallow soil and saprolite layers (Equations 2 and 3). As observed from Figure 4, the majority of Indian coastal groundwater follows a steady-state open flow through the model framework, with isotope fractionation ($^{30}\varepsilon$) between −0.5‰ and −2‰. Within the weathering zone, the formation of clay minerals generally follows the transformation of Al-hydroxides to high surface area amorphous precursors through Si adsorption and subsequent conversion to crystalline clays over time (Oelze et al., 2014). The clay minerals inherit lighter ^{28}Si isotope as a result of a fast unidirectional kinetic adsorption process during the early stages of weathering, followed by a slow re-equilibration, depending on the surface area of precipitating solid and extension of water-rock interaction (Fernandez et al., 2019; Oelze et al., 2014, 2015). The field observations indicate that the $^{30}\varepsilon$ of clay neoformation depends on the mineralogy, with less silicified 2:1 clays such as smectites and vermiculites, exhibiting a smaller $^{30}\varepsilon$ (−0.4‰ to −1.1‰) compared to more silicified kaolinite type clays (−1‰ to −3‰) (Frings, Oelze, et al., 2021; Georg, West, et al., 2009; Opfergelt et al., 2012). Thus, depending on the differences in the dominant clay mineral in the region ($^{30}\varepsilon$) and the extent of Si incorporation (f_{Si}), we can explain the δ^{30}Si range between −0.25 and 2‰, observed in coastal aquifers. In the following subsections, we address alternate mechanisms that can explain the observed heavy ($\delta^{30}\mathrm{Si} > 2$‰) and light ($\delta^{30}\mathrm{Si} < -0.25$‰) silicon isotopic composition in coastal groundwater.

4.2.2. Plant Uptake and Adsorption Processes

An interesting subset of coastal groundwaters exhibits heavy δ^{30}Si values (>2‰) with a $f_{\mathrm{Si}} \leq 0.01$ and Ge/Si < 0.5, pointing to a DSi and Ge-depleted groundwater, fitting more to a Rayleigh model framework. One potential process that could explain the heavy δ^{30}Si signatures and low Ge/Si ratio is adsorption onto pedogenic Fe oxy-hydroxides during percolation through weathering profile, especially in groundwater underlying thick lateritic soil profiles (Figure 3). The relatively fast adsorption kinetics of Si onto Fe oxy-hydroxides in laboratory experiments and also soil porewaters generally follows a Rayleigh model, with a reported $^{30}\varepsilon_{\text{oxyhydroxide-solution}}$

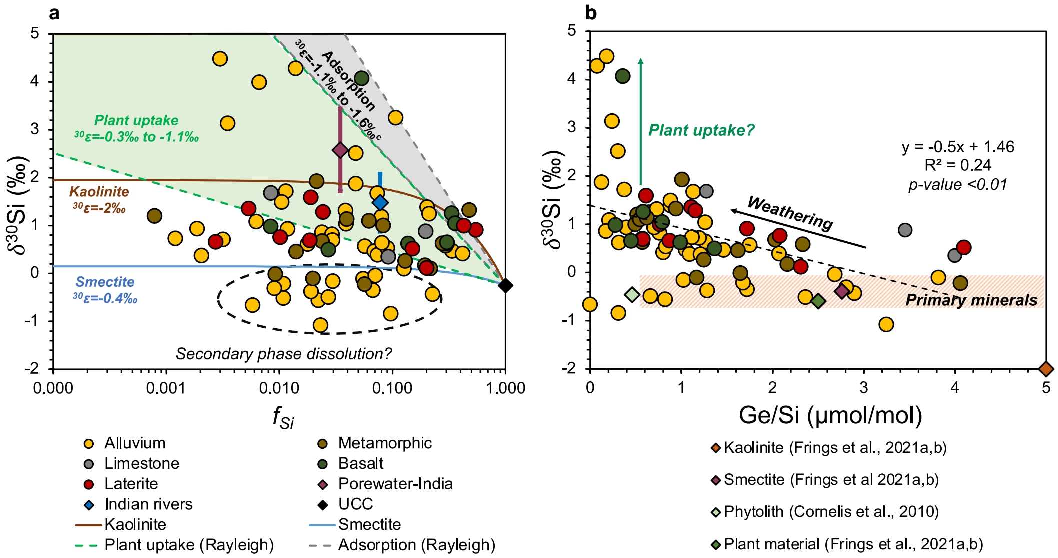

Figure 4. (a) The plot between δ^{30}Si and fraction of silicon remaining in solution (f_{Si}) for all coastal groundwater and river water in Indian subcontinent. The Rayleigh (dashed line) and steady state (solid line) model based evolution of δ^{30}Si in the solution starting from a upper continental crust is depicted for plant uptake ($^{30}\varepsilon = -0.3$‰ to -1.1‰, Frick et al., 2020 and references therein), adsorption ($^{30}\varepsilon = -1.1$‰ to -1.6‰, Delstanche et al., 2009), smectite and kaolinite precipitation ($^{30}\varepsilon = -0.4$‰ -2.0‰ respectively, Frings, Oelze, et al., 2021; Opfergelt et al., 2012). The published soil porewater from South India: Riotte, Meunier et al., 2018; Riotte, Sandhya et al., 2018 and river water: Fontorbe et al., 2013, Frings et al., 2015, Sarath et al., 2022. (b) δ^{30}Si and Ge/Si plot of coastal groundwater. The gray region encompasses the variability in primary minerals Ge/Si and δ^{30}Si composition and identified various endmembers from literature (Cornelis et al., 2010; Frings et al., 2021a, 2021b; Lugolobi et al., 2010; Opfergelt et al., 2012; Riotte, Meunier, et al., 2018).

between -1.1‰ and -1.6‰ for ferrihydrite and goethite, respectively (Delstanche et al., 2009; Riotte, Meunier, et al., 2018). In addition, Ge adsorption as surface complexes onto Fe oxy-hydroxides can also lead to Ge depletion in groundwater (Pokrovski et al., 2006). However, none of the groundwater underlying laterite and ferruginous concretions exhibits δ^{30}Si > 2‰, only two coastal groundwater fits the published $^{30}\varepsilon$ range of adsorption following a Rayleigh fractionation model (Figures 3 and 4). Furthermore, the evidence from field settings indicates that clay formation has dominant control over the Ge/Si ratio of soil rather than adsorption processes (Scribner et al., 2006). Thus, adsorption onto Fe oxy-hydroxides alone cannot explain the observed heavy Si isotopic composition in coastal groundwater.

The heavy δ^{30}Si composition in groundwater and deviation from modeled steady state behavior can also result from substantial plant uptake of DSi from the soil solution. Thus, plant uptake, storage and cycling as phytolith imparts significant control over DSi export and isotopic composition of shallow soil water and aquifer systems (Struyf et al., 2010; Vandevenne et al., 2015). Plant uptake preferentially incorporates a lighter ^{28}Si isotope, enriching the residual solution in heavy ^{30}Si (Frick et al., 2020). The silicon uptake by cultivated crops such as rice (4 wt% Si), sugarcane (1.5%) and maize (0.8%), and associated isotopic fractionation has been extensively documented through hydroponic experiments as well as on the field settings (Frick et al., 2020; Riotte, Meunier, et al., 2018; Sun et al., 2016). For instance, Riotte, Meunier, et al. (2018) observed that soil porewaters (0–20 cm deep) in a paddy field in South India exhibit high δ^{30}Si values, up to 3.9‰, due to the preferential uptake of lighter ^{28}Si isotope from soil solutions, in addition to adsorption in the shallow soil layers. The observed heavy δ^{30}Si signatures in coastal groundwater following a Rayleigh model is consistent with kinetic silicon isotopic fractionation during plant uptake, with documented fractionation factors in crops ranging from -0.3‰ to -1.1‰ (Ding et al., 2005; Frick et al., 2020; Sun et al., 2016). The low Ge/Si ratio (0.23 ± 0.11 μmol/mol) in these groundwaters points to a lack of discrimination or preferential plant uptake of Ge compared to Si, consistent with recent findings from Frings, Schubring, et al. (2021) (Figure 4b). The Ge uptake dynamics depends largely on plant species, and signature recorded in groundwaters can result from a combination of weathering, plant uptake, and remineralization of labile phytolith and non-phytolith Ge pools in soil and saprolite (Frings, Schubring, et al., 2021; Wiche et al., 2018). In regions of low annual rainfall and high water demand, crop irrigation is mainly

19449224, 2025, 8, Downloaded from https://agupubs.onlinelibrary.wiley.com/doi/10.1029/2025GB008706 by Cochrane France, Wiley Online Library on [22/09/2025]. See the Terms and Conditions (https://onlinelibrary.wiley.com/terms-and-conditions) on Wiley Online Library for rules of use; OA articles are governed by the applicable Creative Commons License

sustained through groundwater pumping (Davis et al., 2018). After nearly two decades of drilling millions of borewells, India has the largest groundwater-irrigated cultivated area in the world (almost 44% of the total cultivated area, FAO, 2015). A significant proportion of the irrigated water (up to 50% in rice-cultivated regions) can reach the groundwater systems as irrigation return flow (Dewandel et al., 2008). Thus, in cultivated areas with low rainfall and groundwater irrigation, a substantial part of the return flow, enriched in a ^{30}Si isotope, can infiltrate the underlying groundwater systems (Séraphin et al., 2016; Tulip et al., 2022). These infiltration of return flow to shallow groundwaters, especially in alluvial settings with high hydraulic conductivity and absence of primary silicate minerals, can explain the observed heavy groundwater δ^{30}Si signatures and low Ge/Si (Figures 3 and 4). The interpretation is coherent with observation from large river systems, where exceptionally heavy δ^{30}Si in river water is attributed to contribution from agricultural return flow (Ding et al., 2004; Sarath et al., 2022). However, the extent to which the return flow can impact groundwater δ^{30}Si is subject to additional constraints, such as groundwater storage, lateral connectivity and discharge, water-rock interactions and residence time (Kavil et al., 2024; Maher, 2011).

4.2.3. Dissolution of Secondary Si- Phases in the Weathering Zone

In addition to silicate weathering, DSi in coastal groundwater can originate from dissolution of precipitated secondary minerals (e.g., clays, Fe and Mn oxy-hydroxides) as well as poorly crystalline or amorphous silica (ASi) phases that are ubiquitous in soil and sediments (Cornelis et al., 2011, 2014). Previous works have assigned the light (more negative) δ^{30}Si composition of groundwaters to a shift in Si source from primary mineral weathering to dissolution of secondary smectite-type clays and siliceous pedogenic precipitates such as silcretes (Georg, West, et al., 2009, Georg, Zhu, et al., 2009; Pogge von Strandmann et al., 2014). The coastal groundwater samples from the present study with δ^{30}Si composition lower than UCC values (-0.25 ± 0.16‰, Savage et al., 2013) are restricted to the alluvial aquifer of North East coast, mainly composed of Holocene sediments and an isolated sample from South West coast (Figures 3 and 4). The light ^{28}Si source in this aquifer could be sourced from, (a) complete or partial dissolution of illite and smectite type clays (δ^{30}Si ranges from -0.2 to -1.1‰, Bayon et al., 2018; Frings, Oelze, et al., 2021), (b) dissolution of amorphous Si in aquifer sediments (Cornelis et al., 2014; Desbarats et al., 2017), (c) reductive dissolution of Fe-Mn oxy-hydroxides which is widespread in the shallow aquifers of the Bengal basin (Islam et al., 2004; Varner et al., 2023). The clay mineralogy in alluvial sediments in the North East coast is dominated by illite, kaolinite, smectite and interstratified clays, with the transformation of illite and smectite-type clays to kaolinite occurring in weathering profiles (Singh et al., 1998). The partial dissolution of these pedogenic clay minerals and/or poorly crystalline aluminosilicates formed as a result of dissolution and reprecipitation of pedogenic clays is a source of light ^{28}Si to groundwater (Cornelis et al., 2014). Among the coastal groundwaters with low δ^{30}Si composition, a high Ge/Si value can be indicative of clay mineral dissolution, while a low Ge/Si value indicates dissolution of amorphous phases (clay precursors and phytolith) and/or predominant release of lighter Si through desorption from oxy-hydroxides (Figure 4b). Indeed, recent studies suggest that Ge/Si ratio in the amorphous silica phases is predominantly controlled by subsurface fluid residence times, and fast incorporation kinetics of Si can form a depleted δ^{30}Si reservoir with low Ge/Si ratio (Fernandez et al., 2021). In addition, Holocene alluvial aquifers in Bengal plains are known for their low dissolved oxygen (DO, Figure S2 in Supporting Information S1, data from Kumar et al., 2021), where microbially mediated reductive dissolution of Fe-Mn oxy-hydroxides associated with organic matter occurs, making them prone to arsenic contamination (Islam et al., 2004). The dissolution of Fe-Mn oxy-hydroxides (including amorphous and poorly crystalline oxides and hydrous oxides of Fe(III)) can also release the ^{28}Si-rich silicon adsorbed on these phases into the groundwater systems, leading to a low δ^{30}Si composition (Delstanche et al., 2009). Overall, the δ^{30}Si composition in coastal groundwater lower than the underlying bedrock in alluvial aquifers is mainly sourced from complete or partial dissolution of precipitated secondary phases, including crystalline clays and oxy-hydroxides and amorphous aluminosilicates within the regolith.

4.3. Submarine Groundwater Silicon Fluxes and Isotopic Impact

Dissolved silicon (DSi) in SGD forms a mixture of two components: fresh, terrestrial groundwater (fresh SGD) and recycled saline groundwater (saline SGD) originating from seawater and recirculated through coastal aquifers (Burnett et al., 2006; Moore et al., 2010). The fresh groundwater samples from Indian coastal aquifers (within a few km from the coast) can be considered as representative fresh SGD end members, and resulting Si fluxes a source of DSi to the coastal ocean, which can be estimated as:

19449224, 2025, 8, Downloaded from https://agupubs.onlinelibrary.wiley.com/doi/10.1029/2025GB008706 by Cochrane France, Wiley Online Library on [22/09/2025]. See the Terms and Conditions (https://onlinelibrary.wiley.com/terms-and-conditions) on Wiley Online Library for rules of use; OA articles are governed by the applicable Creative Commons License

Table 2

The Fresh Groundwater Derived Si Fluxes, and Average δ^{30}Si Composition of Fresh Submarine Groundwater Discharge Flux to East Coast (Bay of Bengal) and West Coast (Arabian Sea) of India

	Y_{fsgd} km^3 yr^{-1}	$[DSi]_{fsgd}$ μM	$fSGD_{Si}$ Gmol yr^{-1}	$\delta^{30}Si_{avg}$ ‰
East coast	2.3	666 ± 272	1.5 ± 1.7[a]	0.6 ± 1.1
West coast	1.6	364 ± 288	0.6 ± 0.7[a]	0.9 ± 0.9
Total $fSGD_{Si}$	3.9		2.1 ± 1.7[a]	**0.6 ± 0.8**

Note. The fresh SGD water flux from Luijendijk et al. (2020), the DSi and $\delta^{30}Si_{avg}$ composition from present work. [a]Assuming a 100% uncertainty in fresh SGD flux estimate.

$$fSGD_{Si} = [DSi]_{fgw} * Y_{fsgd} \tag{6}$$

here the $fSGD_{Si}$ is the total Si fluxes in Gmol yr^{-1} to Indian coast through fresh SGD, $[DSi]_{fgw}$ the fresh groundwater endmember dissolved silicon concentration, and Y_{fsgd} is the total coastal fresh SGD water flux. The volumetric flux of fresh SGD along the Eastern and Western Indian coastline from Luijendijk et al. (2020) was used to best represent Y_{fsgd}. The average fresh groundwater DSi and weighted δ^{30}Si along the Eastern coast (Bay of Bengal) and Western coast (Arabian Sea) of India is given in Table 2.

Overall, the estimated total fresh SGD DSi flux from the Indian coastline is 2.1 GmolSi yr^{-1}, which represents <1% of total riverine Si supply to North Indian Ocean (Mangalaa et al., 2017). The fresh SGD DSi flux along the Indian coastline only accounts for 0.3% of the global fresh SGD Si supply, and insignificant compared to the global saline SGD Si flux of 3.1 TmolSi yr^{-1} estimated by Rahman et al. (2019). The discharge weighted δ^{30}Si values of fresh SGD DSi flux from West and East coast of India was 0.68‰ (Table 2), almost 0.8‰ lighter than Indian riverine δ^{30}Si composition of 1.5 ± 0.6‰ (Fontorbe et al., 2013; Frings et al., 2015; Sarath et al., 2022). Despite the low δ^{30}Si composition in fresh coastal groundwater, the overall change in δ^{30}Si composition of Si input fluxes (rivers and groundwater) to the North Indian Ocean is <0.05‰, which is within our analytical uncertainty.

The saline SGD endmember along the Indian coast is more difficult to constrain, given the paucity of saline groundwater endmember in the present study and the non-conservative nature of saline SGD for both DSi and δ^{30}Si values (Figure S4 in Supporting Information S1). The total SGD water flux estimated using radium mass balance from the Indian coast varies from 12 to 115 km^3 yr^{-1}, almost two orders of magnitude higher than fresh SGD water flux (Rengarajan & Sarma, 2015; Yadav et al., 2019). Assuming that the total SGD water flux is entirely of saline groundwater origin and an average saline groundwater DSi composition of 422 ± 165 μM ($n = 10$) from the present study, we can estimate Si fluxes through saline SGD as:

$$sSGD_{Si} = \left([DSi]_{sgw} - [DSi]_{\text{seawater}}\right) * Y_{ssgd} \tag{7}$$

$sSGD_{Si}$ is the DSi flux through saline SGD, $[DSi]_{sgw}$ and $[DSi]_{\text{seawater}}$ is the dissolved silicon concentration in saline groundwater (based on high conductivity and Cl) and seawater (Singh et al., 2015), and Y_{ssgd} is the saline SGD water flux, assumed to be close to reported total SGD flux along the Indian coast. The estimated $sSGD_{Si}$ ranges between 5.1 and 48.6 GmolSi yr^{-1}, 5%–56% of the Si flux exported by Indian rivers (Mangalaa et al., 2017). This is likely an overestimate, given the saline groundwater end member from the present work comprises a mix of saline SGD and fresh SGD. In addition, DSi of saline SGD can be sourced from the dissolution of lithogenic phases and biogenic silica in the subsurface region, and only the lithogenic dissolution can be considered as a new Si source to the coastal ocean (Anschutz et al., 2009; Ehlert, Doering, et al., 2016; Rahman et al., 2019). However, distinguishing new versus recycled Si in saline SGD and understanding the isotopic impact in the coastal ocean is outside the scope of the present work. Overall, we observe a minor impact of fresh groundwater discharge on the silicon isotopic composition and DSi flux to the Indian coastal Ocean.

5. Conclusion

Coastal groundwater from the Indian subcontinent displays large variability in DSi (80–1,350 μM) and δ^{30}Si values (−1.1–4.5 ‰). The average δ^{30}Si value of Indian coastal groundwater (0.8 ± 1.1‰, 1SD, $n = 85$) is comparable to previously published estimate of global groundwater (0.8 ± 0.8‰, $n = 117$), and is significantly lower than the average δ^{30}Si of Indian rivers (1.5 ± 0.6‰, ±1SD, $n = 152$). The observed variability in δ^{30}Si of the groundwater samples do not show any correlation with the aquifer lithology. The coastal alluvial aquifers encompass the largest variability observed in both DSi and δ^{30}Si values. The coastal groundwater from low rainfall regions (<1,200 mm/yr) exhibits on average 0.8‰ heavier δ^{30}Si values compared to high rainfall regions (>2,000 mm/yr), with significantly enriched DSi. The DSi in groundwater is sourced from incongruent weathering of primary silicate minerals, with few alluvial and lateritic aquifers exhibiting signatures of dissolution from secondary phases, for example, clays and amorphous aluminosilicates. Only a few coastal groundwater exhibit

19449224, 2025, 8, Downloaded from https://agupubs.onlinelibrary.wiley.com/doi/10.1029/2025GB008706 by Cochrane France, Wiley Online Library on [22/09/2025]. See the Terms and Conditions (https://onlinelibrary.wiley.com/terms-and-conditions) on Wiley Online Library for rules of use; OA articles are governed by the applicable Creative Commons License

signatures of seawater intrusion, with a fraction of seawater ranging from 4% to 14%, with wide range of DSi (150–680 μM) and δ^{30}Si (0.4–4.5‰) values. The δ^{30}Si composition of most of the coastal groundwater can be explained by a steady-state model, with a dynamic equilibrium between the Si supply and incorporation into secondary Si-bearing phases and a fractionation factor consistent with the formation of smectite and kaolinite type clays. The heaviest δ^{30}Si values (>2‰) followed a Rayleigh model with a low Ge/Si ratio, which can be explained by fractionation during plant uptake in irrigated regions. Finally, we estimated the total Si flux through fresh SGD to be 2.1 Gmol yr^{-1}, which would correspond to <1% of riverine input to the North Indian Ocean and imparts no significant isotopic impact despite having a higher DSi and lower δ^{30}Si values. Overall, groundwater systems form a highly heterogeneous reservoir of Si, exhibiting a 5.5‰ variability in δ^{30}Si composition, incorporating signatures from various abiotic and biotic processes.

Data Availability Statement

The data set for this article can be found online at https://doi.org/10.5281/zenodo.14730770 (Kavil et al., 2025).

Acknowledgments

The current work is funded by CEFIPRA-IFCPAR support (NUNDERGROUND, project #5907). We acknowledge the NIO India team for providing support in the field campaign and groundwater sampling. The authors thank Moustafa Belhadj Senini and Frédéric Candaudap for their support to HR-ICPMS analyses, Hemanth Moger from IFCWS for IC analysis, Pierre Burckel (IPGP) and Irina Djouraev (ALYSES facility IRD-SU) for the help with ICPMS to check for Si chemistry and Mélanie Longchamp (GESE platform, SU) for cation analyses. The authors thank Bobbili Sridevi for their help with the figures. SPK thanked IRD-Campus France for providing a Ph.D. scholarship and constant support to carry out the work. The authors would like to thank M. Benrahmoune (LOCEAN-IPSL) for their help in sample processing and clean lab management at LOCEAN, Sorbonne University.

References

Abraham, K., Opfergelt, S., Fripiat, F., Cavagna, A. J., de Jong, J. T. M., Foley, S. F., et al. (2008). δ^{30}Si and δ^{29}Si determinations on USGS BHVO-1 and BHVO-2 reference materials with a new Configuration on a Nu Plasma Multi-Collector ICP-MS. *Geostandards and Geoanalytical Research*, *32*(2), 193–202. https://doi.org/10.1111/j.1751-908x.2008.00879.x

Aguirre, A. A., Derry, L. A., Mills, T. J., & Anderson, S. P. (2017). Colloidal transport in the Gordon Gulch catchment of the Boulder Creek CZO and its effect on C-Q relationships for silicon. *Water Resources Research*, *53*(3), 2368–2383. https://doi.org/10.1002/2016WR019730

Anschutz, P., Smith, T., Mouret, A., Deborde, J., Bujan, S., Poirier, D., & Lecroart, P. (2009). Tidal sands as biogeochemical reactors. *Estuarine, Coastal and Shelf Science*, *84*(1), 84–90. https://doi.org/10.1016/j.ecss.2009.06.015

Asoka, A., Gleeson, T., Wada, Y., & Mishra, V. (2017). Relative contribution of monsoon precipitation and pumping to changes in groundwater storage in India. *Nature Geoscience*, *10*(2), 109–117. https://doi.org/10.1038/ngeo2869

Baronas, J. J., West, A. J., Burton, K. W., Hammond, D. E., Opfergelt, S., Pogge von Strandmann, P. A. E., et al. (2020). Ge and Si isotope behavior during intense tropical weathering and ecosystem cycling. *Global Biogeochemical Cycles*, *34*(8), e2019GB006522. https://doi.org/10.1029/2019gb006522

Bayon, G., Delvigne, C., Ponzevera, E., Borges, A. V., Darchambeau, F., De Deckker, P., et al. (2018). The silicon isotopic composition of fine-grained river sediments and its relation to climate and lithology. *Geochimica et Cosmochimica Acta*, *229*(May 15), 147–161. https://doi.org/10.1016/j.gca.2018.03.015

Beane, J. E., Turner, C. A., Hooper, P. R., Subbarao, K. V., & Walsh, J. N. (1986). Stratigraphy, composition and form of the Deccan basalts, western Ghats, India. *Bulletin of Volcanology*, *48*(1), 61–83. https://doi.org/10.1007/bf01073513

Berner, R. A., Lasaga, A. C., & Garrels, R. M. (1983). The carbonate-silicate geochemical cycle and its effect on atmospheric carbon dioxide over the past 100 million years. *American Journal of Science*, *283*(7), 641–683. https://doi.org/10.2475/ajs.283.7.641

Bhanja, S. N., Mukherjee, A., Rangarajan, R., Scanlon, B. R., Malakar, P., & Verma, S. (2019). Long-term groundwater recharge rates across India by in situ measurements. *Hydrology and Earth System Sciences*, *23*(2), 711–722. https://doi.org/10.5194/hess-23-711-2019

Bouchez, J., von Blanckenburg, F., & Schuessler, J. A. (2013). Modeling novel stable isotope ratios in the weathering zone. *American Journal of Science*, *313*(4), 267–308. https://doi.org/10.2475/04.2013.01

Bratton, J. F. (2010). The three scales of submarine groundwater flow and discharge across passive continental margins. *The Journal of Geology*, *118*(5), 565–575. https://doi.org/10.1086/655114

Braun, J. J., Descloitres, M., Riotte, J., Fleury, S., Barbiéro, L., Boeglin, J. L., et al. (2009). Regolith mass balance inferred from combined mineralogical, geochemical and geophysical studies: Mule Hole gneissic watershed, South India. *Geochimica et Cosmochimica Acta*, *73*(4), 935–961. https://doi.org/10.1016/j.gca.2008.11.013

Burnett, W. C., Aggarwal, P. K., Aureli, A., Bokuniewicz, H., Cable, J. E., Charette, M. A., et al. (2006). Quantifying submarine groundwater discharge in the coastal zone via multiple methods. *Science of the Total Environment*, *367*(2–3), 498–543. https://doi.org/10.1016/j.scitotenv.2006.05.009

Buvaneshwari, S., Riotte, J., Sekhar, M., Sharma, A. K., Helliwell, R., Kumar, M. M., et al. (2020). Potash fertilizer promotes incipient salinization in groundwater irrigated semi-arid agriculture. *Scientific Reports*, *10*(1), 3691. https://doi.org/10.1038/s41598-020-60365-z

CGWB. (2012). *Aquifer systems of India. Ministry of water Resources*. Govt. of India.

Chakrabarti, R., Mondal, S., Acharya, S. S., Lekha, J. S., & Sengupta, D. (2018). Submarine groundwater discharge derived strontium from the Bengal Basin traced in Bay of Bengal water samples. *Scientific Reports*, *8*(1), 4383. https://doi.org/10.1038/s41598-018-22299-5

Cho, H. M., Kim, G., Kwon, E. Y., Moosdorf, N., Garcia-Orellana, J., & Santos, I. R. (2018). Radium tracing nutrient inputs through submarine groundwater discharge in the global ocean. *Scientific Reports*, *81*(8), 1–7. https://doi.org/10.1038/s41598-018-20806-2

Closset, I., Cardinal, D., Rembauville, M., Thil, F., & Blain, S. (2016). Unveiling the Si cycle using isotopes in an iron-fertilized zone of the Southern Ocean: From mixed-layer supply to export. *Biogeosciences*, *13*(21), 6049–6066. https://doi.org/10.5194/bg-13-6049-2016

Coplen, T. B. (2011). Guidelines and recommended terms for expression of stable-isotope-ratio and gas-ratio measurement results. *Rapid Communications in Mass Spectrometry*, *25*(17), 2538–2560. https://doi.org/10.1002/rcm.5129

Cornelis, J. T., Delvaux, B., Cardinal, D., André, L., Ranger, J., & Opfergelt, S. (2010). Tracing mechanisms controlling the release of dissolved silicon in forest soil solutions using Si isotopes and Ge/Si ratios. *Geochimica et Cosmochimica Acta*, *74*(14), 3913–3924. https://doi.org/10.1016/J.GCA.2010.04.056

Cornelis, J. T., Delvaux, B., Georg, R. B., Lucas, Y., Ranger, J., & Opfergelt, S. (2011). Tracing the origin of dissolved silicon transferred from various soil-plant systems towards rivers: A review. *Biogeosciences*, *8*(1), 89–112. https://doi.org/10.5194/bg-8-89-2011

Cornelis, J.-T., Weis, D., Opfergelt, S., Van Ranst, E., & Dumon, M. (2019). Past and current geochemical conditions influence silicon isotope signatures of pedogenic clay minerals at the soil profile scale, Ethiopia. *Chemical Geology*, *524*, 174–183. https://doi.org/10.1016/j.chemgeo.2019.06.013

19449224, 2025, 8, Downloaded from https://agupubs.onlinelibrary.wiley.com/doi/10.1029/2025GB008706 by Cochrane France, Wiley Online Library on [22/09/2025]. See the Terms and Conditions (https://onlinelibrary.wiley.com/terms-and-conditions) on Wiley Online Library for rules of use; OA articles are governed by the applicable Creative Commons License

Das, K., Ganguly, S., Majumder, P., Chakrabarti, R., & Mukherjee, A. (2025). Interaction of shallow and deep groundwater with a tropical ocean: Insights from radiogenic (87Sr/86Sr) and stable isotope cycling and fluxes. *Journal of Hydrology*, *650*, 132479. https://doi.org/10.1016/j.jhydrol.2024.132479

Davis, K. F., Chiarelli, D. D., Rulli, M. C., Chhatre, A., Richter, B., Singh, D., & DeFries, R. (2018). Alternative cereals can improve water use and nutrient supply in India. *Science Advances*, *4*(7), eaao1108. https://doi.org/10.1126/SCIADV.AAO1108

De, C., & Bhattacharyya, S. (2009). First record of the Recent–subRecent diatomaceous earth from the Gangetic alluvial floodplains of South 24 Parganas, West Bengal, India. *Current Science*, 967–973.

Deepthy, R., & Balakrishnan, S. (2005). Climatic control on clay mineral formation: Evidence from weathering profiles developed on either side of the Western Ghats. *Journal of Earth System Science*, *114*(5), 545–556. https://doi.org/10.1007/BF02702030/METRICS

Delstanche, S., Opfergelt, S., Cardinal, D., Elsass, F., André, L., & Delvaux, B. (2009). Silicon isotopic fractionation during adsorption of aqueous monosilicic acid onto iron oxide. *Geochimica et Cosmochimica Acta*, *73*(4), 923–934. https://doi.org/10.1016/j.gca.2008.11.014

Delvigne, C., Opfergelt, S., Cardinal, D., Delvaux, B., & André, L. (2009). Distinct silicon and germanium pathways in the soil-plant system: Evidence from banana and horsetail. *Journal of Geophysical Research*, *114*(G2). https://doi.org/10.1029/2008jg000899

Derry, L. A., Kurtz, A. C., Ziegler, K., & Chadwick, O. A. (2005). Biological control of terrestrial silica cycling and export fluxes to watersheds. *Nature*, *433*(7027), 728–731. https://doi.org/10.1038/nature03299

Desbarats, A. J., Pal, T., Mukherjee, P. K., & Beckie, R. D. (2017). Geochemical evolution of groundwater flowing through arsenic source sediments in an aquifer system of West Bengal, India. *Water Resources Research*, *53*(11), 8715–8735. https://doi.org/10.1002/2017WR020863

Dessert, C., Dupré, B., Gaillardet, J., François, L. M., & Allègre, C. J. (2003). Basalt weathering laws and the impact of basalt weathering on the global carbon cycle. *Chemical Geology*, *202*(3–4), 257–273. https://doi.org/10.1016/j.chemgeo.2002.10.001

Dewandel, B., Gandolfi, J. M., de Condappa, D., & Ahmed, S. (2008). An efficient methodology for estimating irrigation return flow coefficients of irrigated crops at watershed and seasonal scale. *Hydrological Processes*, *22*(11), 1700–1712. https://doi.org/10.1002/HYP.6738

Dimri, V. P., Srivastava, R. P., & Pandey, O. P. (2023). Measuring Indian coastline using optimum scale: A case study. *Marine Geophysical Research*, *44*(2), 8.

Ding, T., Wan, D., Wang, C., & Zhang, F. (2004). Silicon isotope compositions of dissolved silicon and suspended matter in the Yangtze River, China. *Geochimica et Cosmochimica Acta*, *68*(2), 205–216. https://doi.org/10.1016/S0016-7037(03)00264-3

Ding, T. P., Ma, G. R., Shui, M. X., Wan, D. F., & Li, R. H. (2005). Silicon isotope study on rice plants from the Zhejiang Province, China. *Chemical Geology, In Search of Isotope Biosignatures*, *218*(1), 41–50. https://doi.org/10.1016/j.chemgeo.2005.01.018

Ehlert, C., Doering, K., Wallmann, K., Scholz, F., Sommer, S., Grasse, P., et al. (2016). Stable silicon isotope signatures of marine pore waters – Biogenic opal dissolution versus authigenic clay mineral formation. *Geochimica et Cosmochimica Acta*, *191*, 102–117. https://doi.org/10.1016/j.gca.2016.07.022

Ehlert, C., Reckhardt, A., Greskowiak, J., Liguori, B. T. P., Böning, P., Paffrath, R., et al. (2016). Transformation of silicon in a sandy beach ecosystem: Insights from stable silicon isotopes from fresh and saline groundwaters. *Chemical Geology*, *440*, 207–218. https://doi.org/10.1016/j.chemgeo.2016.07.015

FAO. (2015). *AQUASTAT Country profile – India*. Food and Agriculture Organization of the United Nations (FAO).

FAO. (2022). Food and agriculture organization of the United Nations. Retrieved from http://faostat.fao.org/

Fernandez, N. M., Perez-Fodich, A., Derry, L. A., & Druhan, J. L. (2021). A first look at Ge/Si partitioning during amorphous silica precipitation: Implications for Ge/Si as a tracer of fluid-silicate interactions. *Geochimica et Cosmochimica Acta*, *297*, 158–178. https://doi.org/10.1016/j.gca.2021.01.007

Fernandez, N. M., Zhang, X., & Druhan, J. L. (2019). Silicon isotopic re-equilibration during amorphous silica precipitation and implications for isotopic signatures in geochemical proxies. *Geochimica et Cosmochimica Acta*, *262*, 104–127. https://doi.org/10.1016/j.gca.2019.07.029

Field, C. B., Behrenfeld, M. J., Randerson, J. T., & Falkowski, P. (1998). Primary production of the biosphere: Integrating terrestrial and oceanic components. *Science (80-.)*, *281*(5374), 237–240. https://doi.org/10.1126/science.281.5374.237

Fontorbe, G., De La Rocha, C. L., Chapman, H. J., & Bickle, M. J. (2013). The silicon isotopic composition of the Ganges and its tributaries. *Earth and Planetary Science Letters*, *381*, 21–30. https://doi.org/10.1016/j.epsl.2013.08.026

Frick, D. A., Remus, R., Sommer, M., Augustin, J., Kaczorek, D., & Von Blanckenburg, F. (2020). Silicon uptake and isotope fractionation dynamics by crop species. *Biogeosciences*, *17*(24), 6475–6490. https://doi.org/10.5194/bg-17-6475-2020

Frings, P. J., Clymans, W., Fontorbe, G., De La Rocha, C. L., & Conley, D. J. (2016). The continental Si cycle and its impact on the ocean Si isotope budget. *Chemical Geology*, *425*, 12–36. https://doi.org/10.1016/j.chemgeo.2016.01.020

Frings, P. J., Clymans, W., Fontorbe, G., Gray, W., Chakrapani, G., Conley, D. J., & De La Rocha, C. (2015). Silicate weathering in the Ganges alluvial plain. *Earth and Planetary Science Letters*, *427*, 136–148. https://doi.org/10.1016/J.EPSL.2015.06.049

Frings, P. J., Oelze, M., Schubring, F., Frick, D. A., & von, B. F. (2021). Interpreting silicon isotopes in the critical zone. *American Journal of Science*, *321*(8), 1164–1203. https://doi.org/10.2475/08.2021.02

Frings, P. J., Schubring, F., Oelze, M., & von, B. F. (2021). Quantifying biotic and abiotic Si fluxes in the Critical Zone with Ge/Si ratios along a gradient of erosion rates. *American Journal of Science*, *321*(8), 1204–1245. https://doi.org/10.2475/08.2021.03

Gaillardet, J. D. B. L., Dupré, B., Louvat, P., & Allegre, C. J. (1999). Global silicate weathering and CO_2 consumption rates deduced from the chemistry of large rivers. *Chemical Geology*, *159*(1–4), 3–30. https://doi.org/10.1016/s0009-2541(99)00031-5

Geilert, S., Vroon, P. Z., Roerdink, D. L., Van Cappellen, P., & van Bergen, M. J. (2014). Silicon isotope fractionation during abiotic silica precipitation at low temperatures: Inferences from flow-through experiments. *Geochimica et Cosmochimica Acta*, *142*, 95–114. https://doi.org/10.1016/j.gca.2014.07.003

Georg, R. B., Reynolds, B. C., Frank, M., & Halliday, A. N. (2006a). Mechanisms controlling the silicon isotopic compositions of river waters. *Earth and Planetary Science Letters*, *249*(3–4), 290–306. https://doi.org/10.1016/j.epsl.2006.07.006

Georg, R. B., Reynolds, B. C., Frank, M., & Halliday, A. N. (2006b). New sample preparation techniques for the determination of Si isotopic compositions using MC-ICPMS. *Chemical Geology*, *235*(1–2), 95–104. https://doi.org/10.1016/j.chemgeo.2006.06.006

Georg, R. B., West, A. J., Basu, A. R., & Halliday, A. N. (2009). Silicon fluxes and isotope composition of direct groundwater discharge into the Bay of Bengal and the effect on the global ocean silicon isotope budget. *Earth and Planetary Science Letters*, *283*(1–4), 67–74. https://doi.org/10.1016/j.epsl.2009.03.041

Georg, R. B., Zhu, C., Reynolds, B. C., & Halliday, A. N. (2009). Stable silicon isotopes of groundwater, feldspars, and clay coatings in the Navajo Sandstone aquifer, Black Mesa, Arizona, USA. *Geochimica et Cosmochimica Acta*, *73*(8), 2229–2241. https://doi.org/10.1016/j.gca.2009.02.005

Gleeson, T., Befus, K. M., Jasechko, S., Luijendijk, E., & Cardenas, M. B. (2015). The global volume and distribution of modern groundwater. *Nature Geoscience*, *92*(9), 161–167. https://doi.org/10.1038/ngeo2590

19449224, 2025, 8, Downloaded from https://agupubs.onlinelibrary.wiley.com/doi/10.1029/2025GB008706 by Cochrane France, Wiley Online Library on [22/09/2025]. See the Terms and Conditions (https://onlinelibrary.wiley.com/terms-and-conditions) on Wiley Online Library for rules of use; OA articles are governed by the applicable Creative Commons License

Gopalakrishnan, M., & Kulkarni, S. A. (2007). Agricultural land drainage in India. *Irrigation and Drainage*, *56*(S1), S59–S67. https://doi.org/10.1002/ird.368

Grasse, P., Brzezinski, M. A., Cardinal, D., De Souza, G. F., Andersson, P., Closset, I., et al. (2017). GEOTRACES inter-calibration of the stable silicon isotope composition of dissolved silicic acid in seawater. *Journal of Analytical Atomic Spectrometry*, *32*(3), 562–578. https://doi.org/10.1039/C6JA00302H

Grasshoff, K., Kremlin, K., & Erhardt, M. (1999). *Methods for seawater analysis, third completely revised and extended version* (p. 600). Wiley VCH.

Haynes, R. J. (2017). Significance and role of Si in crop production. *Advances in Agronomy*, *146*, 83–166. https://doi.org/10.1016/BS.AGRON.2017.06.001

Hughes, H. J., Delvigne, C., Korntheuer, M., De Jong, J., André, L., & Cardinal, D. (2011). Controlling the mass bias introduced by anionic and organic matrices in silicon isotopic measurements by MC-ICP-MS. *Journal of Analytical Atomic Spectrometry*, *26*(9), 1892–1896. https://doi.org/10.1039/c1ja10110b

Hughes, H. J., Sondag, F., Santos, R. V., André, L., & Cardinal, D. (2013). The riverine silicon isotope composition of the Amazon Basin. *Geochimica et Cosmochimica Acta*, *121*, 637–651. https://doi.org/10.1016/j.gca.2013.07.040

Islam, F. S., Gault, A. G., Boothman, C., Polya, D. A., Charnock, J. M., Chatterjee, D., & Lloyd, J. R. (2004). Role of metal-reducing bacteria in arsenic release from Bengal delta sediments. *Nature*, *430*(6995), 68–71. https://doi.org/10.1038/nature02638

Jiao, J., & Post, V. (2019). Coastal hydrogeology. *Coastal Hydrogeology*, 1–403. https://doi.org/10.1017/9781139344142

Karl, D. M., & Tien, G. (1992). Magic: A sensitive and precise method for measuring dissolved phosphorus in aquatic environments. *Limnology & Oceanography*, *37*(1), 105–116. https://doi.org/10.4319/lo.1992.37.1.0105

Kavil, S. P., Cardinal, D., Riotte, J., Chakrabarti, R., & Arnaud, D. (2025). Heterogenous Si isotopic composition in coastal groundwater: Controls on dissolved silicon and groundwater discharge along Indian coastline [Dataset]. *Zenodo*. https://doi.org/10.5281/zenodo.14730770

Kavil, S. P., Riotte, J., Chakrabarti, R., Dapoigny, A., Vaury, V., Ruiz, L., & Cardinal, D. (2024). Deep regolith weathering controls δ^{30}Si composition of groundwater under contrasting landuse in tropical watersheds. *Chemical Geology*, *670*, 122370. https://doi.org/10.1016/j.chemgeo.2024.122370

Krishna, M. S., Prasad, M. H. K., Rao, D. B., Viswanadham, R., Sarma, V. V. S. S., & Reddy, N. P. C. (2016). Export of dissolved inorganic nutrients to the northern Indian Ocean from the Indian monsoonal rivers during discharge period. *Geochimica et Cosmochimica Acta*, *172*, 430–443. https://doi.org/10.1016/J.GCA.2015.10.013

Kumar, B. S. K., Viswanadham, R., Kumari, V. R., Rao, D. B., Prasad, M. H. K., Srinivas, N., & Sarma, V. V. S. S. (2021). Spatial variations in dissolved inorganic nutrients in the groundwaters along the Indian coast and their export to adjacent coastal waters. *Environmental Science & Pollution Research*, *28*(8), 9173–9191. https://doi.org/10.1007/s11356-020-11387-7

Kumar, K. R., Pant, G. B., Parthasarathy, B., & Sontakke, N. A. (1992). Spatial and subseasonal patterns of the long-term trends of Indian summer monsoon rainfall. *International Journal of Climatology*, *12*(3), 257–268. https://doi.org/10.1002/joc.3370120303

Kurtz, A. C., Derry, L. A., & Chadwick, O. A. (2002). Germanium-silicon fractionation in the weathering environment. *Geochimica et Cosmochimica Acta*, *66*(9), 1525–1537. https://doi.org/10.1016/s0016-7037(01)00869-9

Lakshmi, D. D., Satyanarayana, A. N. V., & Chakraborty, A. (2019). Assessment of heavy precipitation events associated with floods due to strong moisture transport during summer monsoon over India. *Journal of Atmospheric and Solar-Terrestrial Physics*, *189*, 123–140. https://doi.org/10.1016/j.jastp.2019.04.013

Laluraj, C. M., Gopinath, G., Dinesh Kumar, P. K., & Seralathan, P. (2007). Seasonal variations in groundwater chemistry of a Phreatic coastal and crystalline Terrain of central Kerala, India. *Environmental Forensics*, *7*(4), 335–344. https://doi.org/10.1080/15275920600996305

Larkin, R. G., & Sharp, J. M., Jr. (1992). On the relationship between river-basin geomorphology, aquifer hydraulics, and ground-water flow direction in alluvial aquifers. *GSA Bulletin*, *104*(#12), 1608–1620. https://doi.org/10.1130/0016-7606(1992)104<1608:OTRBRB>2.3.CO;2

Lugolobi, F., Kurtz, A. C., & Derry, L. A. (2010). Germanium–silicon fractionation in a tropical, granitic weathering environment. *Geochimica et Cosmochimica Acta*, *74*(4), 1294–1308. https://doi.org/10.1016/j.gca.2009.11.027

Luijendijk, E., Gleeson, T., & Moosdorf, N. (2020). Fresh groundwater discharge insignificant for the world's oceans but important for coastal ecosystems. *Nature Communications*, *111*(11), 1–12. https://doi.org/10.1038/s41467-020-15064-8

Maher, K. (2010). The dependence of chemical weathering rates on fluid residence time. *Earth and Planetary Science Letters*, *294*(1–2), 101–110. https://doi.org/10.1016/j.epsl.2010.03.010

Maher, K. (2011). The role of fluid residence time and topographic scales in determining chemical fluxes from landscapes. *Earth and Planetary Science Letters*, *312*(1–2), 48–58. https://doi.org/10.1016/j.epsl.2011.09.040

Maldonado, M., López-Acosta, M., Sitjà, C., García-Puig, M., Galobart, C., Ercilla, G., & Leynaert, A. (2019). Sponge skeletons as an important sink of silicon in the global oceans. *Nature Geoscience 2019*, *12*(10), 815–822. https://doi.org/10.1038/s41561-019-0430-7

Mangalaa, K. R., Cardinal, D., Brajard, J., Rao, D. B., Sarma, N. S., Djouraev, I., et al. (2017). Silicon cycle in Indian estuaries and its control by biogeochemical and anthropogenic processes. *Continental Shelf Research*, *148*, 64–88. https://doi.org/10.1016/j.csr.2017.08.011

Manivannan, V., & Elango, L. (2019). Seawater intrusion and submarine groundwater discharge along the Indian coast. *Environmental Science & Pollution Research*, *26*(31), 31592–31608. https://doi.org/10.1007/s11356-019-06103-z

Martin, A., Meredith, K., Baker, A., Norman, M., & Bryan, E. (2021). The evolution of stable silicon isotopes in a coastal carbonate aquifer, Rottnest Island, Western Australia. *Hydrology and Earth System Sciences Discussions*, 1–18.

Mondal, N. C., Singh, V. P., Singh, S., & Singh, V. S. (2011). Hydrochemical characteristic of coastal aquifer from Tuticorin, Tamil Nadu, India. *Environmental Monitoring and Assessment*, *175*(1–4), 531–550. https://doi.org/10.1007/s10661-010-1549-6

Moore, W. S. (2010). The effect of submarine groundwater discharge on the ocean. *Annual Review of Marine Science*, *2*(1), 59–88. https://doi.org/10.1146/annurev-marine-120308-081019

Mortlock, R. A., & Frohlich, P. N. (1987). Continental weathering of germanium: GeSi in the global river discharge. *Geochimica et Cosmochimica Acta*, *51*(8), 2075–2082. https://doi.org/10.1016/0016-7037(87)90257-2

Mukherjee, A., Fryar, A. E., & Thomas, W. A. (2009). Geologic, geomorphic and hydrologic framework and evolution of the Bengal basin, India and Bangladesh. *Journal of Asian Earth Sciences*, *34*(3), 227–244. https://doi.org/10.1016/J.JSEAES.2008.05.011

Oehler, T., Tamborski, J., Rahman, S., Moosdorf, N., Ahrens, J., Mori, C., et al. (2019). DSi as a tracer for submarine groundwater discharge. *Frontiers in Marine Science*, *6*, 563. https://doi.org/10.3389/fmars.2019.00563

Oelze, M. , von Blanckenburg, F., Bouchez, J., Hoellen, D., & Dietzel, M. (2015). The effect of Al on Si isotope fractionation investigated by silica precipitation experiments. *Chemical Geology*, *397*, 94–105.

Oelze, M., von Blanckenburg, F., Hoellen, D., Dietzel, M., & Bouchez, J. (2014). Si stable isotope fractionation during adsorption and the competition between kinetic and equilibrium isotope fractionation: Implications for weathering systems. *Chemical Geology*, *380*, 161–171. https://doi.org/10.1016/j.chemgeo.2014.04.027

19449224, 2025, 8, Downloaded from https://agupubs.onlinelibrary.wiley.com/doi/10.1029/2025GB008706 by Cochrane France, Wiley Online Library on [22/09/2025]. See the Terms and Conditions (https://onlinelibrary.wiley.com/terms-and-conditions) on Wiley Online Library for rules of use; OA articles are governed by the applicable Creative Commons License

19449224, 2025, 8, Downloaded from https://agupubs.onlinelibrary.wiley.com/doi/10.1029/2025GB008706 by Cochrane France, Wiley Online Library on [22/09/2025]. See the Terms and Conditions (https://onlinelibrary.wiley.com/terms-and-conditions) on Wiley Online Library for rules of use; OA articles are governed by the applicable Creative Commons License

Opfergelt, S., & Delmelle, P. (2012). Silicon isotopes and continental weathering processes: Assessing controls on Si transfer to the ocean. *Comptes Rendus Geoscience*, *344*(11–12), 723–738. https://doi.org/10.1016/j.crte.2012.09.006

Opfergelt, S., Georg, R. B., Delvaux, B., Cabidoche, Y. M., Burton, K. W., & Halliday, A. N. (2012). Silicon isotopes and the tracing of desilication in volcanic soil weathering sequences. *Guadeloupe. Chem. Geol.*, *326–327*, 113–122. https://doi.org/10.1016/j.chemgeo.2012.07.032

Pogge von Strandmann, P. A. E., Porcelli, D., James, R. H., van Calsteren, P., Schaefer, B., Cartwright, I., et al. (2014). Chemical weathering processes in the Great Artesian Basin: Evidence from lithium and silicon isotopes. *Earth and Planetary Science Letters*, *406*, 24–36. https://doi.org/10.1016/j.epsl.2014.09.014

Pokrovsky, O. S., Pokrovski, G. S., Schott, J., & Galy, A. (2006). Experimental study of germanium adsorption on goethite and germanium coprecipitation with iron hydroxide: X-Ray absorption fine structure and macroscopic characterization. *Geochimica et Cosmochimica Acta*, *70*(13), 3325–3341. https://doi.org/10.1016/j.gca.2006.04.012

Rahaman, W., & Singh, S. K. (2012). Sr and 87Sr/86Sr in estuaries of western India: Impact of submarine groundwater discharge. *Geochimica et Cosmochimica Acta*, *85*, 275–288. https://doi.org/10.1016/J.GCA.2012.02.025

Rahman, S., Tamborski, J. J., Charette, M. A., & Cochran, J. K. (2019). Dissolved silica in the subterranean estuary and the impact of submarine groundwater discharge on the global marine silica budget. *Marine Chemistry*, *208*, 29–42. https://doi.org/10.1016/j.marchem.2018.11.006

Rajeevan, M., Unnikrishnan, C. K., Bhate, J., Niranjan Kumar, K., & Sreekala, P. P. (2012). Northeast monsoon over India: Variability and prediction. *Meteorological Applications*, *19*(2), 226–236. https://doi.org/10.1002/met.1322

Rengarajan, R., & Sarma, V. V. S. S. (2015). Submarine groundwater discharge and nutrient addition to the coastal zone of the Godavari estuary. *Marine Chemistry*, *172*, 57–69. https://doi.org/10.1016/j.marchem.2015.03.008

Reynolds, B. C., Aggarwal, J., André, L., Baxter, D., Beucher, C., Brzezinski, M. A., et al. (2007). An inter-laboratory comparison of Si isotope reference materials. *J. Anal. At. Spectrom.*, *22*(5), 561–568. https://doi.org/10.1039/b616755a

Reynolds, B. C., Georg, R. B., Oberli, F., Wiechert, U., & Halliday, A. N. (2006). Re-assessment of silicon isotope reference materials using high-resolution multi-collector ICP-MS. *Journal of Analytical Atomic Spectrometry*, *21*(3), 266–269. https://doi.org/10.1039/b515908c

Riotte, J., Meunier, J. D., Zambardi, T., Audry, S., Barboni, D., Anupama, K., et al. (2018). Processes controlling silicon isotopic fractionation in a forested tropical watershed: Mule Hole Critical Zone Observatory (Southern India). *Geochimica et Cosmochimica Acta*, *228*, 301–319. https://doi.org/10.1016/j.gca.2018.02.046

Riotte, J., Sandhya, K., Prakash, N. B., Audry, S., Zambardi, T., Chmeleff, J., et al. (2018). Origin of silica in rice plants and contribution of diatom earth fertilization: Insights from isotopic Si mass balance in a paddy field. *Plant and Soil*, *423*(1–2), 481–501. https://doi.org/10.1007/s11104-017-3535-z

Rodell, M., Velicogna, I., & Famiglietti, J. S. (2009). Satellite-based estimates of groundwater depletion in India. *Nature*, *460*(7258), 999–1002. https://doi.org/10.1038/nature08238

Santos, I. R., Chen, X., Lecher, A. L., Sawyer, A. H., Moosdorf, N., Rodellas, V., et al. (2021). Submarine groundwater discharge impacts on coastal nutrient biogeochemistry. *Nature Reviews Earth and Environment*, *2*(5), 307–323. https://doi.org/10.1038/s43017-021-00152-0

Sarath, P. K., Mangalaa, K. R., Cardinal, D., Gurumurthy, G. P., Dapoigny, A., Sarma, V. V. S. S., & Riotte, J. (2022). Seasonal, weathering and water use controls of silicon cycling along the river flow in two contrasting basins of South India. *Chemical Geology*, *604*, 120883. https://doi.org/10.1016/j.chemgeo.2022.120883

Savage, P. S., Georg, R. B., Williams, H. M., & Halliday, A. N. (2013). The silicon isotope composition of the upper continental crust. *Geochimica et Cosmochimica Acta*, *109*, 384–399. https://doi.org/10.1016/j.gca.2013.02.004

Scribner, A. M., Kurtz, A. C., & Chadwick, O. A. (2006). Germanium sequestration by soil: Targeting the roles of secondary clays and Fe-oxyhydroxides. *Earth and Planetary Science Letters*, *243*(3–4), 760–770. https://doi.org/10.1016/j.epsl.2006.01.051

Séraphin, P., Vallet-Coulomb, C., & Gonçalvès, J. (2016). Partitioning groundwater recharge between rainfall infiltration and irrigation return flow using stable isotopes: The Crau aquifer. *Journal of Hydrology*, *542*, 241–253. https://doi.org/10.1016/J.JHYDROL.2016.09.005

Shamsudduha, M., Uddin, A., Saunders, J. A., & Lee, M. K. (2008). Quaternary stratigraphy, sediment characteristics and geochemistry of arsenic-contaminated alluvial aquifers in the Ganges–Brahmaputra floodplain in central Bangladesh. *Journal of Contaminant Hydrology*, *99*(1–4), 112–136. https://doi.org/10.1016/j.jconhyd.2008.03.010

Singh, L. P., Parkash, B., & Singhvi, A. K. (1998). Evolution of the lower Gangetic Plain landforms and soils in West Bengal, India. *Catena*, *33*(2), 75–104. https://doi.org/10.1016/s0341-8162(98)00066-6

Singh, S. P., Singh, S. K., Bhushan, R., & Rai, V. K. (2015). Dissolved silicon and its isotopes in the water column of the Bay of Bengal: Internal cycling versus lateral transport. *Geochimica et Cosmochimica Acta*, *151*, 172–191. https://doi.org/10.1016/J.GCA.2014.12.019

Struyf, E., Smis, A., Van Damme, S., Garnier, J., Govers, G., Van Wesemael, B., et al. (2010). Historical land use change has lowered terrestrial silica mobilization. *Nature Communications*, *1*, 1–7. https://doi.org/10.1038/ncomms1128

Sun, Y., Wu, L. H., & Li, X. Y. (2016). Experimental determination of silicon isotope fractionation in rice. *PLoS One*, *11*(12), e0168970. https://doi.org/10.1371/JOURNAL.PONE.0168970

Taniguchi, M., Burnett, W. C., Cable, J. E., & Turner, J. V. (2002). Investigation of submarine groundwater discharge. *Hydrological Processes*, *16*(11), 2115–2129. https://doi.org/10.1002/hyp.1145

Tréguer, P., Bowler, C., Moriceau, B., Dutkiewicz, S., Gehlen, M., Aumont, O., et al. (2018). Influence of diatom diversity on the ocean biological carbon pump. *Nature Geoscience*, *11*(1), 27–37. https://doi.org/10.1038/s41561-017-0028-x

Tréguer, P. J., Sutton, J. N., Brzezinski, M., Charette, M. A., Devries, T., Dutkiewicz, S., et al. (2021). Reviews and syntheses: The biogeochemical cycle of silicon in the modern ocean. *Biogeosciences*, *18*(4), 1269–1289. https://doi.org/10.5194/bg-18-1269-2021

Tulip, S. S., Siddik, M. S., Islam, M. N., Rahman, A., Torabi Haghighi, A., & Mustafa, S. M. T. (2022). The impact of irrigation return flow on seasonal groundwater recharge in Northwestern Bangladesh. *Agricultural Water Management*, *266*, 107593. https://doi.org/10.1016/J.AGWAT.2022.107593

Vandevenne, F. I., Delvaux, C., Hughes, H. J., André, L., Ronchi, B., Clymans, W., et al. (2015). Landscape cultivation alters δ30Si signature in terrestrial ecosystems. *Scientific Reports*, *5*(1), 7732. https://doi.org/10.1038/srep07732

Varner, T. S., Kulkarni, H. V., Uddin Bhuiyan, M., Bayani Cardenas, M., Knappett, P. S. K., & Datta, S. (2023). Mineralogical associations of sedimentary arsenic within a contaminated aquifer determined through thermal treatment and spectroscopy. *Minerals*, *13*(7), 889. https://doi.org/10.3390/min13070889

Wedepohl, K. H. (1995). The composition of the continental crust. *Geochimica et Cosmochimica Acta*, *59*, 1217–1232.

White, A. F., & Blum, A. E. (1995). Effects of climate on chemical_ weathering in watersheds. *Geochimica et Cosmochimica Acta*, *59*(9), 1729–1747. https://doi.org/10.1016/0016-7037(95)00078-E

Wiche, O., Székely, B., Moschner, C., & Heilmeier, H. (2018). Germanium in the soil-plant system—A review. *Environmental Science and Pollution Research*, *25*(32), 31938–31956. https://doi.org/10.1007/s11356-018-3172-y

19449224, 2025, 8, Downloaded from https://agupubs.onlinelibrary.wiley.com/doi/10.1029/2025GB008706 by Cochrane France, Wiley Online Library on [22/09/2025]. See the Terms and Conditions (https://onlinelibrary.wiley.com/terms-and-conditions) on Wiley Online Library for rules of use; OA articles are governed by the applicable Creative Commons License

Wille, M., Babechuk, M. G., Kleinhanns, I. C., Stegmaier, J., Suhr, N., Widdowson, M., et al. (2018). Silicon and chromium stable isotopic systematics during basalt weathering and lateritisation: A comparison of variably weathered basalt profiles in the Deccan Traps, India. *Geoderma*, *314*, 190–204.

Worthington, S. R. H., Davies, G. J., & Alexander, E. C. (2016). Enhancement of bedrock permeability by weathering. *Earth-Science Reviews*, *160*, 188–202. https://doi.org/10.1016/j.earscirev.2016.07.002

Yadav, V. B., Jha, S. K., Pulhani, V., & Tripathi, R. M. (2019). Estimation of submarine groundwater discharge using radium mass-balance in Mumbai Harbour Bay, Mumbai, India. *Journal of Radioanalytical and Nuclear Chemistry*, *319*(3), 945–952. https://doi.org/10.1007/S10967-018-6373-4/TABLES/4

Yeghicheyan, D., Aubert, D., Bouhnik-Le, C. M., Chmeleff, J., Delpoux, S., Djouraev, I., et al. (2019). A new interlaboratory characterisation of silicon, rare earth elements and twenty-two other trace element concentrations in the natural river water certified reference material SLRS-6 (NRC-CNRC). *Geostandards and Geoanalytical Research*, *43*, 475–496.

Ziegler, K., Chadwick, O. A., White, A. F., & Brzezinski, M. A. (2005). δ^{30}Si systematics in a granitic Saprolite, Puerto Rico. *Geology*, *33*(10), 817–820. https://doi.org/10.1130/g21707.1

Erratum

The originally published version of this article omitted the contributions for coauthors Damien Cardinal, Jean Riotte, and Arnaud Dapoigny. Their contributions are as follows: Damien Cardinal contributed to Conceptualization, Methodology, Validation, Formal analysis, Investigation, Writing – review & editing, and Project administration; Jean Riotte contributed to Conceptualization, Methodology, Validation, Formal analysis, Investigation, Writing – review & editing, and Project administration; and Arnaud Dapoigny contributed to Methodology, Validation, and Formal analysis. This may be considered the authoritative version of record.